

Late Pleistocene evolution of tides and tidal dissipation

Wilmes, Sophie-Berenice; Pedersen, V. K. ; Schindelegger, Michael; Green, Mattias

Paleoceanography and Paleoclimatology

DOI:

[10.1029/2023PA004727](https://doi.org/10.1029/2023PA004727)

Published: 09/11/2023

Peer reviewed version

[Cyswllt i'r cyhoeddiad / Link to publication](#)

Dyfyniad o'r fersiwn a gyhoeddwyd / Citation for published version (APA):

Wilmes, S-B., Pedersen, V. K., Schindelegger, M., & Green, M. (2023). Late Pleistocene evolution of tides and tidal dissipation. *Paleoceanography and Paleoclimatology*, Article e2023PA004727. <https://doi.org/10.1029/2023PA004727>

Hawliau Cyffredinol / General rights

Copyright and moral rights for the publications made accessible in the public portal are retained by the authors and/or other copyright owners and it is a condition of accessing publications that users recognise and abide by the legal requirements associated with these rights.

- Users may download and print one copy of any publication from the public portal for the purpose of private study or research.
- You may not further distribute the material or use it for any profit-making activity or commercial gain
- You may freely distribute the URL identifying the publication in the public portal ?

Take down policy

If you believe that this document breaches copyright please contact us providing details, and we will remove access to the work immediately and investigate your claim.

Late Pleistocene evolution of tides and tidal dissipation

S.-B. Wilmes¹, V. K. Pedersen², M. Schindelegger³, and J. A. M. Green¹

¹School of Ocean Sciences, Bangor University, Bangor, UK

²Department of Geoscience, Aarhus University, Aarhus, Denmark

³Institute of Geodesy and Geoinformation, University of Bonn, Bonn, Germany

Key Points:

- Tides over the last glacial cycle are explicitly modelled and tidal dissipation ranging back to 430 ka is inferred with regression analysis.
- Enhanced open ocean dissipation ($1.8\text{--}2.5 \times$ present day) occurred during glacial maxima, and near-present-day values during interglacials.
- Peak glacial M_2 tidal dynamics are very sensitive to changes in ice sheet extent, which may influence ocean mixing and glacial climate.

Corresponding author: S.-B. Wilmes, s.wilmes@bangor.ac.uk

Abstract

Studies of the Last Glacial Maximum (LGM; 26.5–19 ka) tides showed strong enhancements in open ocean tidal amplitudes and dissipation rates; however, changes prior to the LGM remain largely unexplored. Using two different ice sheet and sea level reconstructions, we explicitly simulate the evolution of the leading semi-diurnal and diurnal tidal constituents (M_2 , S_2 , K_1 and O_1) over the last glacial cycle with a global tide model. Both sets of simulations show that global changes, dominated by the Atlantic, take place for the semi-diurnal constituents, while changes for the diurnal constituents are mainly regional. Irrespective of the reconstruction, open ocean dissipation peaks during the sea level lowstands of MIS 2 (~20 ka) and MIS 4 (~60 ka), although dissipation values prior to MIS 2 are sensitive to differences in reconstructed ice sheet extent. Using the statistically significant relationship between global mean sea level and dissipation, we apply regression analysis to infer open ocean and shelf dissipation, respectively, over the last four glacial cycles back to 430 ka. Our analysis shows that open ocean tidal energy was probably increased for most of this period, peaking during glacial maxima, and returning to near-present-day values during interglacials. Due to tidal resonance during glacial phases, small changes in bathymetry could have caused large changes in tidal amplitudes and dissipation, emphasising the need for accurate ice margin reconstructions. During glacial phases, once global mean sea level decreased by more than ~100 m, the amount of open ocean tidal energy available for ocean mixing approximately doubled.

1 Introduction

Tides are important for numerous processes in the ocean: in coastal areas, they shape intertidal ecosystems and morphology. In shelf-sea areas, tidal dynamics determine the location of tidal mixing fronts, which separate seasonally stratified waters from year-round mixed waters (e.g., Simpson & Pingree, 1978). This partitioning is important for shelf sea ecosystems, biogeochemical cycles and the export of CO_2 from the shelf seas to the deep ocean (Thomas et al., 2004). In the open ocean, tidally driven mixing supplies approximately half (~1 TW) of the energy necessary to sustain the large-scale meridional overturning circulation (Wunsch & Ferrari, 2004; Ferrari & Wunsch, 2009). Recent work (Wilmes et al., 2021) demonstrated that, for the the Last Glacial Maximum (26.5–19 thousand years before present (ka); the LGM hereafter), strong increases in tidal mixing (due to the sea level lowstand and associated changes in tidal dynamics) could be constrained from sediment carbon isotopes. As sea level index points (SLIPs) in coastal areas are generally related to a given high or low tide level and not mean sea level, knowledge of past tidal range changes is important for reconstructing past sea levels (see e.g., Ward et al., 2016). Furthermore, marine terminating ice sheet dynamics are affected by tidal dynamics which influence grounding line movement (Milillo et al., 2017; Batchelor et al., 2023), basal melting (Milillo et al., 2017; Anselin et al., 2023), ice shelf flexure (Walker et al., 2013) and ice flow (Bindschadler et al., 2003; Anandakrishnan, 2003; Gudmundsson, 2007).

Reconstructions of global tides and tidal dissipation during the Quaternary (2.58 Ma to present) have generally focused on the last ~25 thousand years (kyr) encompassing the LGM, the deglacial (19–11.7 ka), and the Holocene (11.7 ka to present) (Egbert et al., 2004; Uehara et al., 2006; Griffiths & Peltier, 2008, 2009; Green, 2010; Wilmes & Green, 2014; Wilmes et al., 2019, 2022; Sulzbach et al., 2023). These investigations showed surprising results: the tides were strongly enhanced in the Atlantic during the LGM, especially in the semi-diurnal band, with tidal energy dissipation (i.e., the loss of energy of the tide to bed friction and to the internal tide) for the M_2 tide a factor 2–3 larger than at present in the open ocean. Changes in the North Atlantic are thought to have been particularly strong with amplitudes tripling with respect to present and exceeding 6 m in the Labrador Sea during the LGM (Griffiths & Peltier, 2008, 2009; Wilmes & Green, 2014). These amplifications resulted from changes in ocean basin shape driven by the ~130 m global mean sea level (GMSL) drop and associated increases in ice sheet extent. Together, these factors rendered the Atlantic more conducive to resonant amplification of the semi-diurnal tides, thus leading to substantial increases in amplitudes and tidal energy dissipation (e.g., Egbert et al., 2004; Green, 2010). Through the deglacial and the

Holocene, energy losses in the deep ocean decreased dramatically whilst the shelf seas (which were emersed during the LGM) re-flooded and became more tidally energetic.

On longer time scales, covering the middle and late Pleistocene (~ 770 – 11.7 ka), sea level fluctuated by 130 – 145 m as climate cycled between glacial and interglacial phases (e.g., Fox-Kemper et al., 2021). During this period, ice sheet extent followed a saw-tooth shaped pattern: glacial phases were generally characterised by a long-term gradual cooling culminating in a glacial maximum with peak ice sheet extent and sea level lowstands. Subsequently, climate warmed rapidly and transitioned to interglacial conditions, with climate similar to, or warmer than the pre-industrial. GMSL attained highstands of up to $+15$ m and ice sheet extent was similar to, or less than present. The last glacial period spanned from the end of the Last Interglacial (LIG; 130 – 115 ka; Marine Isotope Stage (MIS) 5e) to the onset of the Holocene, with significant variations in global mean sea level (Waelbroeck et al., 2002; Siddall et al., 2003; Lambeck, 2004; Spratt & Lisiecki, 2016)(see Figure 1a). During the early part of the glacial period (MIS 5 d–a; 115 – 71 ka), GMSL fluctuated between relative high- and lowstands of -9 and -50 m, respectively (e.g., Creveling et al., 2017). During MIS 4 (71 – 57 ka), a GMSL lowstand of around -80 m was reached. Thereafter, GMSL rose to a relative highstand during MIS 3 (57 – 29 ka), though the exact magnitude remains debated (e.g., Dalton et al., 2022). The GMSL lowstand of ~ -130 m during the LGM (MIS 2) was reached between 26.5 and 20 ka (Clark et al., 2009; Lambeck et al., 2014; Peltier et al., 2015; Gowan et al., 2021). At the onset of the deglacial period (19 – 11.7 ka), GMSL first rose gradually, then more rapidly by around 100 m until the early Holocene (~ 8 ka) when present-day levels were reached. Because tides are sensitive to water depth and changes in ocean basin shape and they behave like shallow water waves, it is expected that they are affected by these large sea level changes, as previously seen for the period spanning from the LGM to the present (e.g., Egbert, 2004; Uehara et al., 2006; Green, 2010; Wilmes & Green, 2014; Wilmes et al., 2022; Sulzbach et al., 2023).

In this work, we aim to extend our knowledge of Pleistocene tidal dynamics back to ~ 430 ka. First, we explicitly model tides over the past glacial cycle covering the period from the LIG to present using two different ice sheet and sea level reconstructions, thus expanding the work in Wilmes et al. (2022) to the entire last glacial cycle. Second, because no spatially and temporally highly resolved global sea level and ice sheet reconstructions exist for the previous multiple glacial cycles, we use the last glacial cycle simulations together with uniform sea level change simulations and extrapolate tidal energy dissipation back to 430 ka based on linear regression analysis. We aim to (1) produce global spatially-varying dissipation estimates for the last glacial cycle which can be used for modelling of the late Pleistocene climate and ocean circulation; and (2) improve our understanding of late Pleistocene tidal dynamics which is relevant for, e.g., SLIPs, ice sheet dynamics, or shelf sea oceanographic processes.

2 Methods

2.1 Tide model

For the tide model simulations, we use the Oregon State Tidal Inversion Software (thereafter OTIS; see Egbert et al., 2004; Green & Nycander, 2013; Wilmes et al., 2019, for details) in its forward mode. OTIS has been used for numerous paleotide (e.g., Egbert et al., 2004; Wilmes & Green, 2014; Green & Huber, 2013; Green et al., 2017) and future tide applications (e.g., Carless et al., 2016; Wilmes et al., 2017; Pickering et al., 2017; Hayden et al., 2020). OTIS solves the linearised shallow water equations (e.g., Hendershott, 1972):

$$\frac{\partial \mathbf{U}}{\partial t} + \mathbf{f} \times \mathbf{U} = -gH\nabla(\zeta - \zeta_{EQ} - \zeta_{SAL}) - \mathbf{F} \quad (1)$$

$$\frac{\partial \zeta}{\partial t} = -\nabla \cdot \mathbf{U} \quad (2)$$

where \mathbf{U} is the depth integrated volume transport, H denotes water depth, \mathbf{f} is the Coriolis vector, g is the gravitational constant, ζ denotes tidal elevation, ζ_{EQ} stands for the equilibrium tidal elevation, and ζ_{SAL} is the tidal elevation due to self-attraction and loading (SAL; i.e., the combined effects of gravitational attraction among the water masses, seafloor deformation, and associated changes in the

112 gravity potential). $\mathbf{F} = \mathbf{F}_B + \mathbf{F}_{IT}$ represents frictional losses due to bed friction (\mathbf{F}_B) and tidal
 113 conversion (\mathbf{F}_{IT}). The former is represented by the standard quadratic law:

$$114 \quad \mathbf{F}_B = C_d \mathbf{u} |\mathbf{u}| \quad (3)$$

115 where $C_d = 0.003$ is a drag coefficient, and \mathbf{u} tidal velocity. The energy losses to the internal tide,
 116 $\mathbf{F}_{IT} = C_{IT} \mathbf{U}$, depend on a conversion coefficient C_{IT} given by (Zaron & Egbert, 2006; Green &
 117 Huber, 2013)

$$118 \quad C_{IT}(x, y) = \gamma \frac{(\nabla H)^2 N_b \bar{N}}{8\pi\omega} \quad (4)$$

119 where $\gamma = 37.5$ is a scaling factor (see Zaron & Egbert, 2006, for more details), N_b is the buoyancy
 120 frequency at the sea-bed, \bar{N} is the vertical average of the buoyancy frequency, and ω is the frequency
 121 of the tidal constituent under evaluation. γ was tuned following the process described in Wilmes
 122 and Green (2014) to both minimise present-day amplitude root-mean square errors against TPXO9
 123 and fit TPXO9 dissipation values. Horizontally uniform abyssal stratification was assumed which is
 124 parameterized by the buoyancy frequency N through $N(z) = N_0 e^{(-z/1300)}$ with $N_0 = 5.24 \times 10^{-3}$.
 125 Sensitivity simulations in Wilmes and Green (2014) and Schmittner et al. (2015), where the sensitivity
 126 to glacial interglacial stratification changes was explored, showed that dissipation is rather insensitive
 127 to glacial-interglacial stratification changes. Tidal dissipation associated with the combined action
 128 of \mathbf{F}_B and \mathbf{F}_{IT} is calculated following the energy balance method outlined in Ray et al. (2003).

129 **2.2 Simulations**

130 **2.2.1 Last Glacial Cycle**

131 In our tide model runs, we represent the ice sheet and sea level history over the last glacial
 132 cycle with two different ice sheet reconstructions, one external reconstruction by Gowan et al. (2021)
 133 and one derived by us, using a global gravitationally self-consistent sea level model. For the latter,
 134 we simulate sea level based on the ICE6G_C ice history (Argus et al., 2014; Peltier et al., 2015)
 135 that spans the period 122 ka to present with a temporal resolution of 250–500 yrs prior to 21 ka,
 136 1000 yrs up to 32 ka, and 2000 yrs thereafter (referred to as “ICE-6G” from this point onwards. In
 137 the sea level model, we compute the time-varying deformation of a rotating, Maxwell viscoelastic
 138 Earth model with a depth-dependent Earth structure (e.g., Kendall et al., 2005; Milne & Mitrovica,
 139 1996). For consistency with the global ICE6G_C ice model, we adopt the corresponding VM5a
 140 depth-dependent Earth model to represent global Earth structure (Argus et al., 2014; Peltier et al.,
 141 2015). Importantly for our application here, the sea level model includes migrating shorelines and
 142 the inundation of water into regions previously covered by marine ice (Mitrovica & Milne, 2003).
 143 The model formulation is solved using a pseudo-spectral numerical scheme up to spherical harmonic
 144 degrees and order 256 (Kendall et al., 2005).

145 As an alternative to the boundary conditions derived from the ICE6G_C ice sheet history,
 146 we use the ice sheet and sea level reconstruction from Gowan et al. (2021). Gowan et al. (2021)
 147 presented a global high-resolution ice sheet reconstruction for the period 80 ka to present. The
 148 reconstruction is consistent with ice physics but was inferred independently of far-field sea level
 149 and $\delta^{18}\text{O}$ proxy records (i.e., based on ice sheet margins and constructed to be consistent with
 150 simple ice sheet physics). The sea level predictions provided by Gowan et al. (2021) also rely on a
 151 global gravitationally self-consistent sea level model (SELEN; e.g., Spada & Stocchi, 2007) with a
 152 depth-dependent Earth structure, as well as shoreline migration. These reconstructions have a lower
 153 temporal resolution of 2500 yrs.

154 For our study, both ice sheet reconstructions and the associated sea level change fields were
 155 interpolated to the finite-difference grid of OTIS ($1/8^\circ$ spacing in both latitude and longitude) and
 156 added to the present-day base topography RTopo-2 (Schaffer et al., 2016). We note that both the ice
 157 sheet history and the solid Earth structure, and thus sea level, differ between the two approaches. For
 158 the ICE-6G sea levels, tide runs were performed at 2000-year intervals. Each simulation was run with
 159 M_2 , S_2 , K_1 and O_1 equilibrium tidal forcing and a simplified SAL scheme that sets $\zeta_{SAL} = \beta\zeta$, with
 160 $\beta = 0.1$. The computational grid extends all the way to 89°N , where it is bounded by an artificial

	RMSE (cm)			Modelled dissipation (TW)			TPXO9 dissipation (TW)		
	deep	shelf	global	deep	shelf	global	deep	shelf	global
M_2	3.7	10.1	4.7	1.2	1.3	2.5	0.8	1.5	2.4
S_2	2.0	4.4	2.3	0.2	0.3	0.5	0.2	0.3	0.5
K_1	1.1	3.2	1.4	0.2	0.2	0.4	0.1	0.2	0.3
O_1	1.2	2.6	1.4	0.1	0.1	0.2	0.1	0.1	0.2

Table 1. Present-day control evaluation. Amplitude root-mean square errors (RMSE) against TPXO9 for the deep ocean ($h > 500$ m), shelf seas ($h < 500$ m), and the global ocean. Integrated dissipation values (diss.) are also given for the deep ocean ($h > 500$ m), shelf seas ($h < 500$ m), and the global ocean for both the present-day control and for TPXO9.

vertical wall eliminating the need for open boundaries. Although these two simplifications (SAL and pole cap) potentially suppress resonant behavior of the Arctic Ocean during the LGM (Griffiths & Peltier, 2009), the errors incurred in terms of globally integrated dissipation are expected to be small (Sulzbach et al., 2023) and simulations with an iterative SAL scheme carried out previously (Wilmes et al., 2022) show very similar results for the deglacial.

Additionally, to separate the effect of GMSL changes from land-ocean boundary changes and effects of non-uniform sea level change, we conducted tidal simulations with uniform sea level changes. Here, sea level was uniformly changed from -135 m to $+20$ m in steps of 5 m. Again, RTopo-2 at $1/8^\circ \times 1/8^\circ$ grid spacing was used as the present-day base topography and the simulations were carried out for M_2 and K_1 .

The present-day control simulation (i.e., for 0 ka) was benchmarked against the global tidal solution TPXO9-atlas-v5 (<https://www.tpxo.net/global/tpxo9-atlas>) by calculating amplitude root-mean square errors and comparing globally integrated dissipation values; see Table 1. Evidently, the model yields realistic solutions for both diurnal and semi-diurnal tidal constituents.

2.2.2 Multiple glacial cycles (430 ka–present)

Owing to the lack of global bathymetry, ice sheet and sea level reconstructions spanning multiple glacial cycles, it is currently not possible to explicitly model tidal dynamics prior to the LIG. We therefore take a different, novel approach to infer tidal dissipation prior to the last glacial cycle to gain a first-order understanding of tidal dynamics during this period. We first establish regression models between GMSL and globally integrated deep ocean and shelf sea dissipation rates, respectively, using the three simulation sets described above, i.e., runs for (1) the last glacial cycle based on ICE-6G, (2) the last glacial cycle based on Gowan et al. (2021), and (3) uniform GMSL changes. Using the global sea level reconstruction by Spratt and Lisiecki (2016) (thereafter SL16), each regression model is then used to infer tidal dissipation for open ocean and shelf ocean dissipation back to 430 ka. Because GMSL is driven by global ice volume changes, and the ice sheet volume changes over the last multiple glacial cycles generally follow similar patterns (e.g., waxing and waning of the Laurentide and Fennoscandinavian ice sheets) (e.g., Batchelor et al., 2019), we here use GMSL as a proxy for the combined spatially-varying ice volume and sea level changes which drive the changes in the tides. The different bathymetry reconstructions provide a measure of the uncertainty introduced by the differing ice margins.

For the regression models, we chose a polynomial regressions of order two between GMSL (sl) and globally integrated tidal dissipation (D) for the deep and shelf ocean (D_{deep} and D_{shelf}), respectively, for each tidal constituent. The quadratic fit accounts for non-linear interactions between GMSL and dissipation due to e.g., resonance effects. The relationship between GMSL and tidal

dissipation thus takes the following form:

$$D_{deep} = \beta_{d0} + \beta_{d1}sl + \beta_{d2}sl^2 \quad (5)$$

$$D_{shelf} = \beta_{s0} + \beta_{s1}sl + \beta_{s2}sl^2 \quad (6)$$

$$D_{total} = D_{deep} + D_{shelf} \quad (7)$$

where $\{\beta_{d0}, \beta_{d1}, \beta_{d2}\}$ and $\{\beta_{s0}, \beta_{s1}, \beta_{s2}\}$ represent the regression coefficients for deep and shelf dissipation for each set of model simulations, respectively. We calculated regression coefficients for the relationships between GMSL and deep and shelf dissipation for all three sets of tide runs, respectively. If the relationship between sl^2 and D was not significant at the 95% confidence level, the order of the polynomial was reduced to one (i.e., linear regression). The relationship between sl and D_{deep} and D_{shelf} , respectively, was calculated separately because, in general, deep and shelf dissipation behaved in an anti-correlated manner in relation to GMSL (i.e., when GMSL decreases, open ocean dissipation increases and shelf dissipation decreases). The globally integrated dissipation D_{total} is given by the sum of D_{deep} and D_{shelf} .

Using each regression model and the SL16 GMSL reconstruction, we then calculated time series of late Pleistocene deep, shelf, and total dissipation. Dissipation values were predicted for each constituent (M_2 , S_2 , K_1 and O_1) as per Eqs. (5)–(7) and associated standard deviations (σ) were deduced by applying the laws of variance propagation:

$$\sigma_{D_{deep}}^2 = \sigma_{\beta_{d0}}^2 + \sigma_{\beta_{d1}}^2 sl^2 + (\beta_{d1}^2 + (2\beta_{d2}sl)^2) \sigma_{sl}^2 + \sigma_{\beta_{d2}}^2 sl^4 \quad (8)$$

$$\sigma_{D_{shelf}}^2 = \sigma_{\beta_{s0}}^2 + \sigma_{\beta_{s1}}^2 sl^2 + (\beta_{s1}^2 + (2\beta_{s2}sl)^2) \sigma_{sl}^2 + \sigma_{\beta_{s2}}^2 sl^4 \quad (9)$$

$$\sigma_{D_{total}}^2 = \sigma_{D_{deep}}^2 + \sigma_{D_{shelf}}^2 \quad (10)$$

where sl denotes GMSL from the SL16 reconstruction with the provided formal error σ_{sl} , and $\sigma_{\beta\dots}$ denotes the standard deviations associated with the respective regression coefficients.

3 Results

3.1 The last glacial cycle: LIG to present

3.1.1 Ice sheet and sea level evolution

The two ice sheet and sea level reconstructions show pronounced differences during large parts of the last glacial cycle (Fig. 1a and 2). In the following, we will focus on the differences between the two. For a detailed presentation of the two ice sheet and sea level reconstructions, see Gowan et al. (2021), and Argus et al. (2014), Peltier et al. (2015) and Pedersen et al. (in prep). Whilst a fully developed Laurentide Ice Sheet is present from around 100 ka in ICE-6G, a similarly extensive ice sheet is not formed until after 65 ka in the Gowan reconstruction. This leads to a GMSL offset of ~ 30 m between the two reconstructions during late MIS 5 and early MIS 4 and large differences in shallow shelf sea area. During the MIS 4 peak glaciation, the ICE-6G Laurentide Ice Sheet is slightly more extensive than in Gowan, with the Laurentide Ice Sheet and the Cordilleran Ice Sheet joined up, whereas they remain separated in Gowan. However, the Gowan reconstruction has more extensive ice around Antarctica. Overall, as a result of these differences, ICE-6G sea levels show a slightly lower and earlier MIS 4 GMSL lowstand than Gowan. However, whilst GMSL leading into MIS 4 is similar, there are large regional differences in sea level due to the differences in ice history. The largest differences in ice sheet extent and sea level between the two reconstructions are seen during MIS 3. ICE-6G shows extensive Northern Hemisphere ice sheets throughout MIS 3 whereas in Gowan, ice sheet extent is strongly reduced around 40 ka, with the Fennoscandinavian and Cordilleran Ice Sheets mostly melted and the Laurentide Ice Sheet strongly reduced. These discrepancies lead to an offset in GMSL of around 60 m in the middle of MIS 3 and shelf sea area is approximately doubled in Gowan in comparison to ICE-6G. Towards the LGM, both reconstructions show expanding ice sheets and a drop in GMSL. ICE-6G shows slightly more extensive Northern Hemisphere ice sheets, whereas Gowan shows a stronger expansion of the Antarctic ice sheet margins. The ICE-6G sea level lowstand occurs around 26 ka, whereas, for Gowan, it does not take place until 20 ka, and is

242 around 20 m less than for ICE-6G. From 20 ka to present, both simulations show a similar GMSL
243 evolution. However, again, there are pronounced differences in regional sea levels (locally, > 50 m
244 offsets) due to differences in instantaneous ice sheet loading but also ice history.

245 **3.1.2 Amplitude evolution**

246 Large changes in tidal amplitudes (regionally in excess of 4 m) occur over the last glacial cycle for
247 both sea level reconstructions, but, owing to the discrepancies in sea level and ice sheet history, there
248 are pronounced offsets between the tidal histories (see Figs. 3 and 4 for total amplitude changes). In
249 the following, we discuss how each constituent contributes to the total amplitude changes, focusing
250 the description on the areas that show the largest changes and laying the emphasis on M_2 , which
251 shows the largest absolute changes.

252 For the ICE-6G simulations, M_2 amplitudes (Figure S1 in Supporting Information S1) show
253 levels similar to present-day during the LIG. But, M_2 amplitudes in the North Atlantic, in the Weddell
254 Sea and to a lesser extent in the South Atlantic and in the Gulf of Panama rapidly increase at the
255 termination of the LIG and onwards. A further increase in amplitudes in these areas occurs from
256 68 ka onward towards the sea level lowstand around 60 ka, where, additionally, the Arctic shows
257 large tidal amplitudes (> 3 m in the Chukchi Sea). After 60 ka, the enhancements persist, albeit at a
258 slightly reduced level. During the transition to the LGM, North Atlantic amplitudes increase further
259 to peak round 20 ka, however, Weddell Sea amplitudes are much reduced in comparison to MIS 3
260 because of the more extensive grounded ice in the bay. During the deglacial, pronounced drops in
261 North Atlantic and Arctic M_2 amplitudes take place, and by 8 ka tidal amplitude reach near-present
262 day levels.

263 For the Gowan simulations, M_2 amplitudes (Figure S5 in Supporting Information S1) between
264 80 ka and 72.5 ka show similar levels to present, apart from considerably larger amplitudes in the
265 Weddell and Ross Sea area. As the sea level lowstand around 60 ka is approached, North Atlantic
266 amplitudes strongly increase. These enhancements persist (albeit at a smaller magnitude) until ~55
267 ka, after which the North Atlantic oscillates between periods of larger and smaller M_2 amplitudes
268 with peaks around 45 ka, 37.5 ka and 32.5 ka. Notable are also strongly increased tides in the Ross
269 Sea between 50 and 40 ka. Large North Atlantic amplitudes develop towards the LGM and during
270 the early to mid deglacial (peaking around 17.5 ka and persisting until 12.5 ka). During LGM, strong
271 enhancements in Arctic tides can also be seen.

272 For the ICE-6G runs, S_2 amplitudes (Figure S2 in Supporting Information S1) are similar to
273 present at the end of the LIG. During the early glacial, Labrador Sea and North Atlantic amplitudes
274 increase, but the increases are less pronounced than for M_2 . Furthermore, large S_2 amplitudes occur
275 in the Coral Sea (NE Australia). The two sea level lowstands (~60 ka and LGM) are characterised
276 by large North Atlantic tides and strong enhancements in Arctic S_2 amplitudes. S_2 amplitudes in
277 the Gowan simulations (Figure S6 in Supporting Information S1) follow a similar picture as M_2
278 amplitudes albeit with a lower magnitude. Notable is that Arctic S_2 amplitudes enhancements are
279 much reduced in the Gowan simulations and are only present during the middle of the LGM.

280 In the ICE-6G runs, K_1 and O_1 tidal changes (Figure S4 in Supporting Information S1) are
281 mainly regional. During the sea level lowstands around 62 ka and during the LGM, Pacific shelf
282 seas (Sea of Okhotsk, South China Sea and Banda Sea) become resonant. During the remainder of
283 the last glacial cycle, amplitudes remain close to their present-day levels.

284 Similarly, both K_1 and O_1 amplitudes are characterised by mainly regional changes in the
285 Gowan simulations (Figures S7 and S8 in Supporting Information S1). During periods of sea level
286 lowstands (~62.5–55 ka and 27.5–15 ka), increased amplitudes can be seen around Antarctica and in
287 the shelf seas of the Pacific, whereas other parts of the ocean seem rather insensitive to the large sea
288 level and ocean basin shape changes.

3.1.3 Dissipation evolution

For M_2 , global open ocean dissipation in the ICE-6G simulation is at near-present-day values during the LIG (Figure 1b). It approximately doubles over a period of ~ 10 kyr between 120 and 110 ka to ~ 2 TW when N and S Atlantic dissipation increases (see Fig. 5). It remains elevated at this level until around 70 ka when dissipation rises by a further 25% (0.5 TW) driven by Arctic and N and S Atlantic dissipation increases. Open ocean dissipation remains at these elevated values peaking around 65 ka, 40 ka and during the LGM, with only a small dip occurring around 28 ka. From 68 ka to 30 ka, open ocean dissipation in the Southern Ocean more than doubled in the ICE-6G runs driven by increases in the Weddell Sea area which increases Southern Hemisphere dissipation to levels greater than in the Northern Hemisphere (Figure S9 in Supplementary Information S1). During MIS 4 to MIS 2, dissipation increases around the European Shelf, in the Labrador Sea, Denmark Strait, Norwegian Sea, along the mid-Atlantic ridge, in the Arctic Basin and also in the South Atlantic. In contrast, the Gowan simulations show near present-day open ocean dissipation values (apart from around Antarctica which increases Southern Hemisphere dissipation; Figure S9 in Supplementary Information S1) prior to the sea level lowstand around 60 ka when they increase by $\sim 50\%$ during the sea level lowstand through Atlantic enhancements (see Fig. 6). Thereafter, dissipation decreases slightly, but oscillates through three distinct troughs and peaks. It is notable that Hudson Bay & Strait dissipation is significantly anti-correlated with North Atlantic dissipation, suggesting that when Hudson Bay & Strait lies dry or is ice covered, North Atlantic dissipation peaks. Towards the LGM, dissipation increases again, and reaches its peak during the early deglacial phase with a 90% increase relative to present driven by increases in Atlantic (especially North Atlantic) and Arctic dissipation, whereas in the ICE-6G simulations, dissipation in the Southern Hemisphere decreases—in contrast to the Gowan simulations.

Despite the large differences in shelf area (see Fig. 1a), the evolution of shelf sea dissipation is relatively similar between the two sets of simulations. Between 120 and 70 ka, shelf dissipation is at levels similar to present. With the decrease in sea level towards the lowstand around 60 ka, shelf dissipation decreases by $\sim 40\%$ and remains reduced until the onset of the Holocene with values halved with respect to present during the LGM. In the Gowan simulation, around 40 ka, the values increase to present-day levels and then decrease again to their LGM minimum. Overall, for M_2 , the simulations suggest that open ocean dissipation was enhanced for most of the last glacial period, but that the exact magnitude is dependent on the sea level and ice sheet evolution. Less M_2 energy was lost in the shelf seas between 70 ka and the onset of the Holocene and more M_2 energy dissipated in the open ocean. Overall, the results from the ICE-6G simulations suggest that total dissipation was larger than present for most of the glacial cycle, on average 25% (maximum $\sim 40\%$), whereas for the Gowan simulations which only extend back to 80 ka, the average increase was only 7% (maximum 28%).

For S_2 (Figure 1c), in contrast, total dissipation is lower than present for most of the glacial cycle, except for the Holocene (for ICE-6G, the average decrease is 15%). This is driven by pronounced decreases in shelf sea dissipation which are strongest between 70 ka and the mid-deglacial. The magnitude of the decrease (up to 60% with respect to present) is slightly larger in the ICE-6G simulations due to the larger reduction in shelf area. Deep dissipation is slightly elevated (20–30%) in the ICE-6G simulation, but reduced with respect to present (apart from the LGM period) in the Gowan simulation.

For K_1 (Figure 1d), the overall pattern is similar to S_2 , with total dissipation being slightly reduced for most of the glacial cycle (for ICE-6G by $\sim 10\%$) driven by lower levels of shelf sea dissipation. Again, open ocean dissipation in the ICE-6G simulation is enhanced between 70 ka and the onset of the Holocene and shelf sea dissipation remains reduced; whereas in the Gowan simulation, there are two distinct peaks situated around the sea level lowstands at 60 ka and the LGM. Between the lowstands, open ocean dissipation and shelf sea dissipation returns to present-day values.

For O_1 (Figure 1e), the shelf sea dissipation signal is similar to S_2 and K_1 , but the decreases are compensated by increases in open ocean dissipation, such that total dissipation remains at values

341 near present for most of the glacial cycle and an increase of up to 38% in total dissipation occurs
 342 during the peak of the LGM (cf. Sulzbach et al., 2023).

343 Overall, this means that, for the Gowan simulations, globally integrated dissipation, on average,
 344 was close to present-day levels between 80 ka and present, but for the ICE-6G simulations, total
 345 dissipation over the whole glacial cycle was on average $\sim 15\%$ larger than at present (Figure 1f).
 346 Deep dissipation in the ICE-6G runs was 57% greater on average (80% larger between 66 ka and
 347 16 ka), and raised by 34% in the Gowan simulation. For shelf dissipation the mean reductions for
 348 ICE-6G and Gowan are 22 and 24%, respectively.

349 3.2 Tidal evolution over the last 430 kyr

350 3.2.1 Relationship between GMSL and tidal dissipation

351 For the ICE-6G simulations, open ocean dissipation is highly and significantly anti-correlated
 352 with GMSL for all constituents ($r < -0.88$ for all constituents)—i.e., when sea level drops, open
 353 ocean dissipation increases (see Fig 7). For shelf dissipation, similarly high magnitude signifi-
 354 cantly positive correlations emerge ($r > 0.95$) but the relationship is opposite, i.e., decreasing sea
 355 levels reduce shelf dissipation. In contrast, total dissipation shows a weaker albeit still significant
 356 relationship with GMSL, owing to the opposing relationships of open ocean and shelf dissipation.
 357 For M_2 and O_1 , total dissipation is anti-correlated with GMSL (i.e., larger dissipation with lower
 358 GMSL), whereas for S_2 and K_1 we observe the reverse. For the Gowan simulations, correlations
 359 generally have the same sign as the correlations in the ICE-6G simulations, but with slightly reduced
 360 magnitudes. Dissipation from the uniform sea level drop simulations shows similarly high negative
 361 correlations between GMSL and open ocean dissipation as the ICE-6G simulations, and highly
 362 positive correlations between GMSL and shelf dissipation.

363 Next, we evaluate the polynomial regression fit between GMSL and both shelf and open ocean
 364 dissipation for each tidal constituent for all three sets of simulations, respectively (see Fig. 8). For
 365 open ocean dissipation, all constituents apart from S_2 show $r > 0.95$ between actual and estimated
 366 dissipation values, and for shelf dissipation all regression models can explain more than 89% of the
 367 variability. For the Gowan simulations, the regression fit is good for the diurnal constituents but
 368 shows a slightly less good fit for the semi-diurnal constituents ($r = 0.65$ and $r = 0.68$ for M_2 and S_2 ,
 369 respectively). Regression-based total dissipation for each constituent (Figure S10 in Supplementary
 370 Information S1), calculated as the sum of D_{deep} and D_{shelf} from the regression models for each
 371 constituent, compares well with explicitly modelled dissipation ($r > 0.90$) for ICE-6G. A similarly
 372 good fit can be achieved with the uniform SL simulations. However, it is notable that for M_2 ,
 373 the uniform SL simulations show only very small variations in dissipation (< 0.2 TW for GMSL
 374 variations between -135 m to $+20$ m) in comparison to the ICE-6G simulations (> 1.1 TW for
 375 GMSL variations between -130 m and $+3$ m), as increases in open ocean dissipation increases
 376 are balanced by decreases in shelf dissipation. For the Gowan simulations, the regression models
 377 are able to reproduce explicitly modelled values for all constituents well, apart from M_2 , where the
 378 regression model produces near constant total dissipation values and correlation between explicitly
 379 and regression total modelled dissipation is not significant.

380 Interestingly, pronounced differences emerge in the relationship between GMSL and M_2 open
 381 ocean dissipation (Fig. 8) across the sets of simulations. Whilst both ICE-6G and the uniform
 382 SL simulations show a strongly negative relationship, the slope of the relationship is very different,
 383 with the uniform SL simulations showing much smaller increases in dissipation than the ICE-6G
 384 simulations for the equivalent GMSL decrease. The Gowan simulations fall somewhat between the
 385 two other estimates. These differences may reflect the strong control exerted by coastline positions on
 386 the large M_2 open ocean tides (e.g., Arbic et al., 2009; Green, 2010; Wilmes et al., 2019), especially
 387 as differences in ice sheet extent and non-uniform sea level changes cause offsets in coastlines in
 388 comparison to the uniform sea level drop case. On the other hand, the non-uniform sea level changes
 389 driven by GIA processes, which are especially pronounced close to ice sheets where we generally
 390 see the largest tides, may also be contributing to these differences (see, e.g., Arbic et al., 2008).

3.2.2 Dissipation estimates over the last 430 kyr

Following on, we now use the SL16 sea level curve and associated errors (Fig. 9a) to infer dissipation back to 430 ka by applying all three regression models. The SL16 sea level curve shows large variability in GMSL with sea level fluctuating between highstands of ~ -8 m and $+16$ m during the interglacials and sea level lowstands of 98–129 m during glacial maxima. On average, GMSL was 54 m lower than present over the last 431 ka, according to SL16. The SL16 GMSL estimate compares well with the ICE-6G derived GMSL for the last glacial cycle ($r = 0.98$, $p = 0.00$) (Fig. 9a). Small offsets (~ 15 m) can be seen during MIS 5, when climate entered into the last glacial phase. However, large differences emerge between SL16 and Gowan, which are especially pronounced during MIS 3 and late MIS 5.

Regression-inferred dissipation values for the last glacial cycle closely follow the explicitly modelled values both for ICE-6G and Gowan (Fig. 9b–k). The largest offsets occur when the sea level curves of ICE-6G and Gowan disagree with SL16, e.g., around the relative sea level highstands at 100 ka and 80 ka for ICE-6G, and during MIS 3 for Gowan. The disparities are most pronounced for M_2 open ocean dissipation. Looking back over the last four glacial cycles, the ICE-6G regression model suggests that M_2 open ocean dissipation was strongly increased with respect to present—on average by 120%, i.e., more than doubled—apart from during interglacial phases. When GMSL drops by more than 100 m, M_2 open dissipation increases on average by a factor 2.6. For the Gowan model, the mean M_2 open ocean enhancements (36%) are less pronounced and open ocean dissipation during sea level lowstands increased by a factor 1.7. These Gowan change estimates are very similar to those obtained using the uniform SL model (Figure S11 in Supplementary Information S1). For shelf dissipation, all three models give very similar results, estimating the mean decrease in dissipation to be around 20% over the last 430 kyr. Total M_2 dissipation averaged over the last 430 kyr was between 3% (uniform SL), 5% (Gowan) and 37% (ICE-6G) greater than at present. For the other constituents, average total dissipation changes are less pronounced, generally within $\pm 25\%$. However, considerable fluctuations in the partitioning of tidal energy between the open ocean and the shelf seas can be seen; with S_2 , K_1 and O_1 open ocean dissipation increasing during glacial periods and decreasing towards present-day values during interglacials, respectively, and shelf dissipation behaving in an opposing manner. Taken together, these results suggest that globally integrated open ocean dissipation was on average between 28% (Gowan) and 85% (ICE-6G) greater than at present, with enhancements by a factor 1.5 to 2.2 during sea level lowstands and values similar to present during highstands. However, it is worth noting that the exact magnitude of the estimated changes is dependent on the specific sea level (and ice sheet) model adopted.

4 Discussion and Implications

Our simulations are able to reproduce the findings of other studies for the LGM, deglacial and Holocene (Arbic et al., 2004; Uehara et al., 2006; Griffiths & Peltier, 2008, 2009; Green, 2010; Wilmes & Green, 2014; Wilmes et al., 2019, 2022), but also provide the first continuous estimates of tides and tidal dissipation for the last 430 kyr, thus expanding our knowledge on tidal dynamics prior to the LGM.

Our results show that, apart from interglacial phases, tides and tidal dissipation were different from present during most of this extended time period, covering multiple glacial-interglacial cycles. Changes were especially pronounced for the M_2 tidal constituent, which displays near-resonant behaviour during the LGM (Arbic et al., 2004; Uehara et al., 2006; Griffiths & Peltier, 2008, 2009; Green, 2010; Wilmes & Green, 2014; Wilmes et al., 2019). Our results show that the M_2 tide in the open ocean was strongly enhanced with respect to present for most of the last glacial cycles, whereas for the constituents S_2 , K_1 and O_1 the relative enhancements were smaller and confined to periods with the lowest sea levels. Peak open ocean amplitudes and dissipation occurred when GMSL dropped below 70 m. Notably, for the LGM and for both the ICE-6G and Gowan simulations, peak dissipation values do not coincide with the lowest sea levels and greatest ice sheet extent but reach their maximum 4–5 kyr after the lowstand as the ice begins to recede and sea level begins to increase (at 22 ka for ICE-6G and 15 ka for Gowan). This is likely related to the location of grounded

442 ice margins and thus regional shelf area which in turn affects resonance properties of the glacial
443 Atlantic (see experiments in Wilmes et al., 2019, which show that reduced Weddell Sea ice extent
444 increases Atlantic dissipation by ~ 1 TW).

445 However, there are considerable differences between the two reconstructions for the last glacial
446 cycle, and thus differences in the simulated tides. Whilst the two reconstructions show relatively
447 similar GMSL and ice sheet extent from 20 ka to present and agree during the two peak glaciations
448 (LGM and MIS 4), they strongly differ in ice sheet extent and GMSL during MIS 3 (55 ka to 25
449 ka) and late MIS 5 (80 ka to 65 ka) (see Fig. 2). The ICE-6G reconstruction shows an extensive
450 Laurentide ice sheet (LIS) from 80 ka and Fennoscandia is largely covered by ice from 70 ka onwards.
451 In contrast, the Gowan reconstruction has extensive ice sheets over North America and Fennoscandia
452 only during the glacial periods around 60 ka and the LGM. Ice sheet extent leading up to these periods
453 (80–65 ka and 55–30 ka) is much reduced in comparison to ICE-6G, and restricted to smaller more
454 localised ice caps (see Fig. 2). This leads to pronounced differences in local relative sea level of over
455 100 m and GMSL offsets of over 65 m between the two reconstructions during MIS 3 (see Figure
456 1a and Fig. 2). GMSL during MIS 3 is subject to high uncertainty with sea level estimates for this
457 periods remaining debated (e.g., Pico et al., 2016, 2017; Dalton et al., 2016, 2022). Because of a lack
458 of direct markers of GMSL prior to the LGM, pre-LGM GMSL is often inferred from proxy records
459 such as $\delta^{18}\text{O}$ from benthic foraminifera (e.g., Waelbroeck et al., 2002) or planktonic foraminifera
460 (Shakun et al., 2015), from speleotherms in the Red Sea (Grant et al., 2014; Rohling et al., 2009)
461 and compilations from multiple statistically analysed records (Spratt & Lisiecki, 2016). However,
462 because $\delta^{18}\text{O}$ carries the imprint of both global ice-volume and ocean-temperature changes, the
463 records need to be corrected for temperature changes to obtain sea level curves (e.g., De Boer et
464 al., 2014). Large offsets in MIS 3 GMSL of 30–60 m have been found between ice sheet based
465 reconstructions (e.g., Pico et al., 2016, 2017; Dalton et al., 2016; Gowan et al., 2021; Dalton et
466 al., 2022) and records inferred from marine $\delta^{18}\text{O}$ (e.g., Waelbroeck et al., 2002; Spratt & Lisiecki,
467 2016), with ice sheet reconstructions suggesting that (i) the Laurentide Ice Sheet during MIS 3 was
468 much less extensive than previously thought and (ii) GMSL was ~ 30 – 50 m lower than at present
469 (Pico et al., 2016, 2017; Dalton et al., 2016, 2022). This implies that, for MIS 3, the Gowan sea level
470 and ice sheet reconstruction may be more appropriate as it captures the relative sea level highstand
471 and reduced ice sheet extent.

472 By comparing the ICE-6G and Gowan tide simulations for the LGM, it becomes apparent how
473 sensitive the tidal dynamics are to relative small changes in bathymetry, i.e., changes in both sea level
474 and ocean basin shape (e.g., through ice sheet extent changes) when in a near-resonant state. At 20
475 ka, M_2 open ocean dissipation differs by 0.5 TW between the ICE-6G and Gowan simulation, despite
476 a very similar GMSL drop of 116 m and 120 m, respectively. Experiments in Wilmes et al. (2019)
477 showed that LGM M_2 tidal dynamics were remarkably insensitive to offsets in GMSL (± 10 m) but
478 that changes in the location of the land-ocean boundaries could have dramatic effects (e.g., altering
479 ice sheet extent in the Weddell Sea led to a > 1 TW change in M_2 dissipation). This is also shown
480 when comparing the uniform SL change simulations with those that have realistic glacial land ocean
481 boundaries (1.8 TW versus 2.5 and 2.0 TW for ICE-6G and Gowan, respectively). Comparing the
482 ICE-6G and Gowan 20 ka bathymetries (see Fig. 2) shows that the Gowan reconstruction has more
483 ice around the margins of the Laurentide and the Greenland Ice Sheets but also around the margins
484 of Antarctica. Furthermore, whilst GMSL is very similar between the two reconstructions, regional
485 sea levels in the Labrador Sea differ by over 50 m (Fig. 2) which may also influence tidal dynamics
486 and contribute to the dissipation offsets. It is also worth noting that the LGM sea level lowstand
487 does not occur at the same time in the two reconstructions: in ICE-6G, the lowest sea levels occur
488 around 26 ka, whereas for Gowan they occur at 20 ka, and the ICE-6G lowstand is 10 m lower than
489 in Gowan (-130 m versus -120 m).

490 This work and that of Wilmes et al. (2019) demonstrate that small changes in land-ocean
491 boundaries, e.g., through changes in ice sheet extent, could dramatically alter open ocean tidal
492 energy dissipation on the order of ± 1 TW. In experiments using the intermediate climate model
493 UVic (Schmittner et al., 2015; Wilmes et al., 2019, 2021), changes of this order of magnitude
494 correspond to a ~ 2 – 4 Sv change in AMOC strength. These strong sensitivities in glacial tides could

495 cause rapid changes in the amount of tidal energy available for ocean mixing which, in turn, could
496 impact ocean circulation and thus climate. Feedbacks between tides, ice sheet extent, ocean mixing,
497 and climate may be a modulating factor for glacial climate, especially for period such as Heinrich
498 events, where ice loss from Hudson Strait has been postulated to have affected tidal dynamics and
499 vice versa (e.g., Arbic et al., 2004; Velay-Vitow et al., 2020). For instance, in the Gowan simulations,
500 between 60 ka and 25 ka, fluctuations in M_2 open ocean dissipation can be seen which appear
501 related to Hudson Bay & Strait dissipation, thus suggesting that Hudson Bay & Strait ice cover may
502 affect (North) Atlantic tidal energy availability. Furthermore, the large tides along the ice sheet
503 margins—both for the Antarctic and Northern Hemisphere ice sheets—may have contributed to the
504 rapid ice sheet retreat linked with the deglacial increase in sea level (Gomez et al., 2020; Batchelor
505 et al., 2023), for example, through ice shelf tidal flexure and crevasse formation (e.g., Olinger et al.,
506 2019).

507 Because the sea level simulations used for the last glacial cycle include no ice history prior to
508 122 ka (ICE-6G) and 80 ka (Gowan), the oldest timeslices (i.e., LIG for ICE-6G and late MIS 5 for
509 Gowan) are likely associated with the largest errors, as each time step is affected by previous ice sheet
510 and sea level history. For example, because no ice history was present for the penultimate glacial
511 maximum, the exact sea levels and thus tides during the LIG, are likely subject to larger errors. It
512 is also possible that, due to ice history 'memory' from previous glaciations, tidal dynamics moving
513 into a glaciation may behave differently than during the deglacial phase. However, at present, due to
514 a lack of global high resolution ice sheet reconstructions beyond the LIG, it is not possible to evaluate
515 this point. Another source of uncertainty is the relatively low temporal resolution of the ice sheet
516 histories (2.5 kyr for Gowan throughout the last glacial cycle and 2 kyr prior to 32 ka for ICE-6G,
517 ≤ 1 kyr after 32 ka) and for ICE-6G, the horizontal resolution of the ice sheets ($1/2^\circ \times 1/2^\circ$). It is
518 conceivable that the adopted histories lack small scale ice sheet and bathymetry fluctuations, which,
519 during tidally resonant states, could have led to large short-term regional and supraregional shifts in
520 tidal dynamics.

521 Simulations of climate during the last glacial cycle or parts thereof generally neglect transient
522 changes in tidal energy input to ocean mixing and hold mixing rates constant at the present-day or
523 glacial state (e.g., Menviel et al., 2017; Pöppelmeier et al., 2023). However, this work emphasises
524 that tidal dissipation strongly varied between glacial and interglacial phases and that large short-
525 term variations may have occurred during transitions into and out of glacial phases. The explicitly
526 simulated glacial cycle tidal dissipation timeslices can be used to adjust vertical mixing in transient
527 climate model simulations. These also account for regional responses in dissipation which may
528 differ from the global mean (e.g., during MIS 3 dissipation enhancements in the Southern
529 Hemisphere are greater than in the Northern Hemisphere which stands in contrast to full glacial
530 conditions during the LGM).

531 **5 Conclusion**

532 In this study, we have simulated tidal amplitudes and tidal dissipation for the last glacial cycle
533 encompassing the LIG to present. In addition, we have estimated tidal dissipation for the last four
534 glacial cycles spanning back to 430 ka. Our findings suggest that tides likely differed from present
535 during most glacial phases, with maximum tidal amplitudes and open ocean dissipation occurring
536 during sea level lowstands due to the resonant properties of the glacial ocean with regards to the
537 semi-diurnal tidal forcing. Additionally, we discovered that during glacial phases, semi-diurnal tides,
538 particularly M_2 , were highly sensitive to sea level and ice sheet extent, which remain uncertain prior
539 to the LGM. These results are of wider relevance as they indicate that the availability of tidal energy
540 during the late Pleistocene strongly differed from the present, potentially impacting ocean mixing,
541 and thus ocean circulation and climate in the past.

542 **6 Open Research**

543 The data used in this study are available using the following links: Gowan et al. (2021) ice sheet
544 and sea level reconstruction <https://doi.pangaea.de/10.1594/PANGAEA.905800>, ICE-6G

545 ice sheet reconstruction <https://www.atmosph.physics.utoronto.ca/~peltier/data.php>,
546 TPXO9 tidal atlas <https://www.tpxo.net/global/tpxo9-atlas> and RTopo-2 <https://doi>
547 [.pangaea.de/10.1594/PANGAEA.856844](https://doi.org/10.1594/PANGAEA.856844). The tidal simulations and relevant grid files together
548 with the Matlab routines necessary to read the data are available at the repository Zenodo via
549 [doi:10.5281/zenodo.8147509](https://doi.org/10.5281/zenodo.8147509) (<https://zenodo.org/record/8147509>) with open access (Wilmes
550 et al., 2023).

551 **Acknowledgments**

552 SBW and JAMG were funded through NERC grant NE/S009566/1. MS was supported by the German
553 Research Foundation (DFG, Project no. 451039647). Simulations were done on Supercomputing
554 Wales through Bangor University.

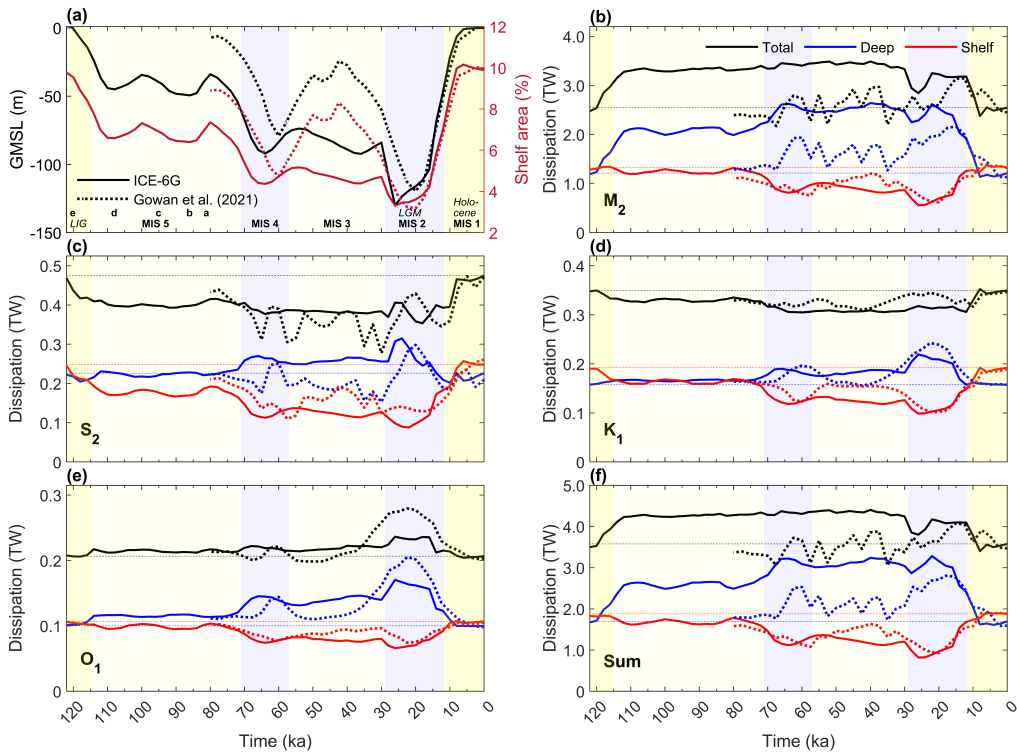


Figure 1. (a) Global mean sea level (black line) and shelf area (in % of global ocean area) for ICE-6G (solid lines) and Gowan (2021) (dotted lines). Marine isotope stages 1 to 5 are indicated by shading and labels above the timeline. For MIS 5, letters indicate substages. Interglacial periods are highlighted by yellow shading. Italic labels show climate periods: LIG = Last Interglacial; LGM = Last Glacial Maximum. (b–e) Dissipation for the constituents M_2 , S_2 , K_1 and O_1 , respectively. Open ocean (deep) dissipation is plotted in blue, shelf sea dissipation in red and globally integrated dissipation in black. ICE-6G values are plotted with solid lines and Gowan (2021) values with dashed lines. (f) same as (b–e) but for the sum of the constituents. The dashed thin straight lines give present-day values as a reference.

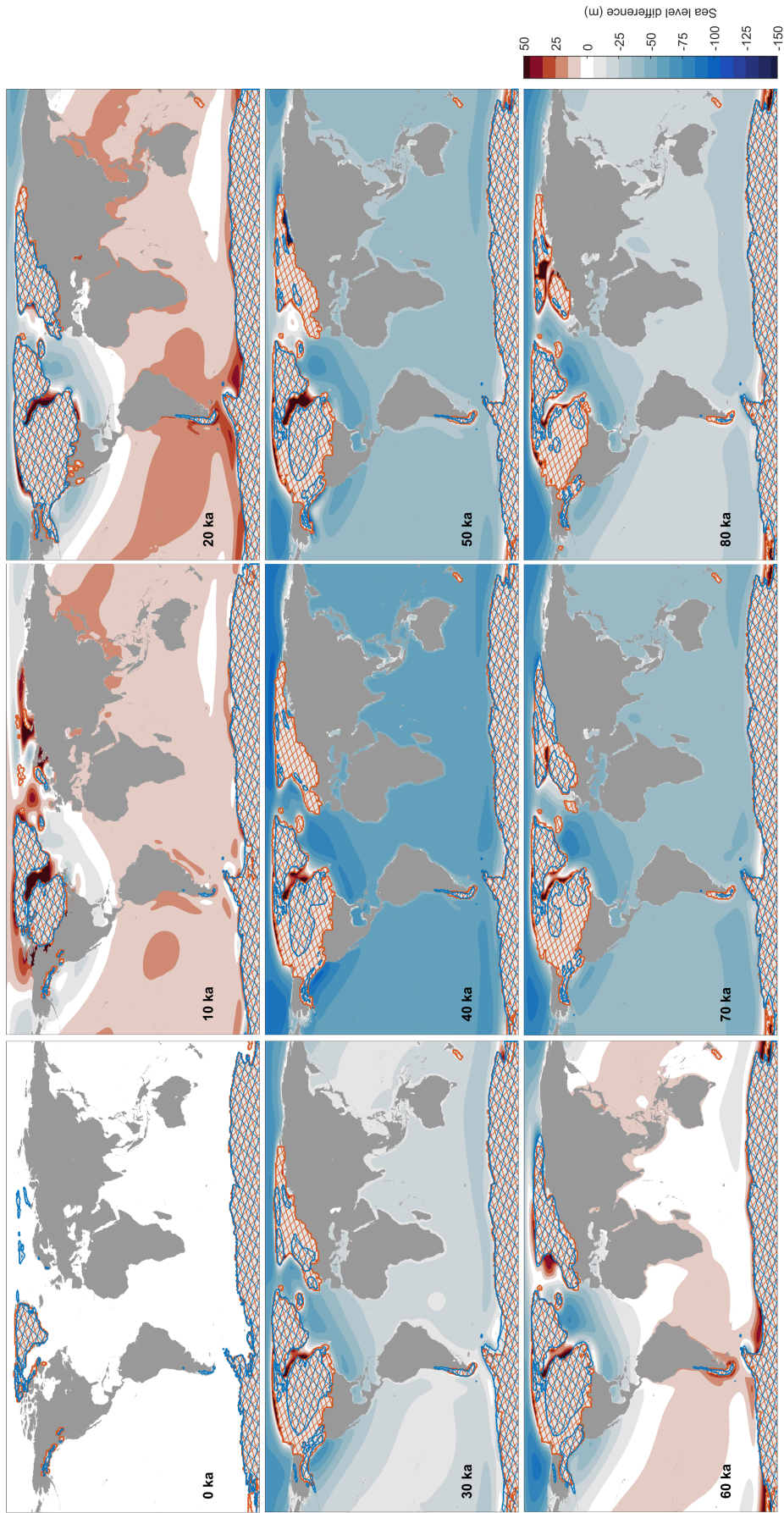


Figure 2. Differences in sea level and ice sheet extent between ICE-6G bathymetries and Gowan et al. (2021) for selected timeslices. Differences in sea level change plotted as ICE-6G minus Gowan (i.e., blue colours indicate lower sea levels in ICE-6G and red colours higher sea levels in ICE-6G than in Gowan). ICE-6G ice sheet extent is indicated with orange hashing, Gowan ice sheet extent is given with blue hashing.

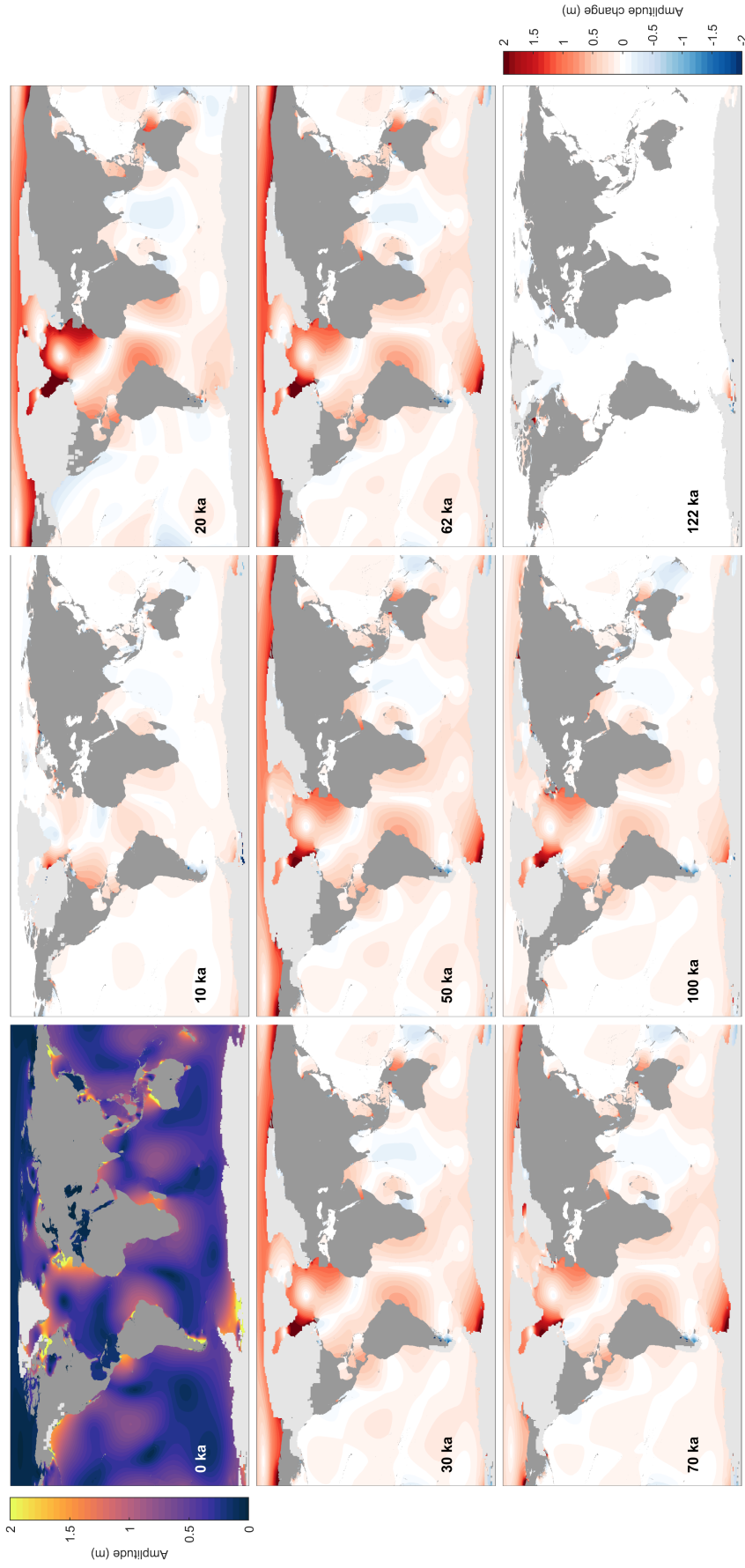


Figure 3. (top left) Present-day tidal amplitudes plotted as the square-root of the sum of the squared amplitudes (\sim equivalent to mean high water levels) of the constituents M_2 , S_2 , K_1 and O_1 . (remaining panels) Tidal amplitude (shown as the square-root of the sum of the squared amplitudes of the constituents M_2 , S_2 , K_1 and O_1) changes with respect to present for selected time slices over the last glacial cycle for the ICE-6G simulations. Land is shaded in dark grey and land ice coverage is indicated in light grey.

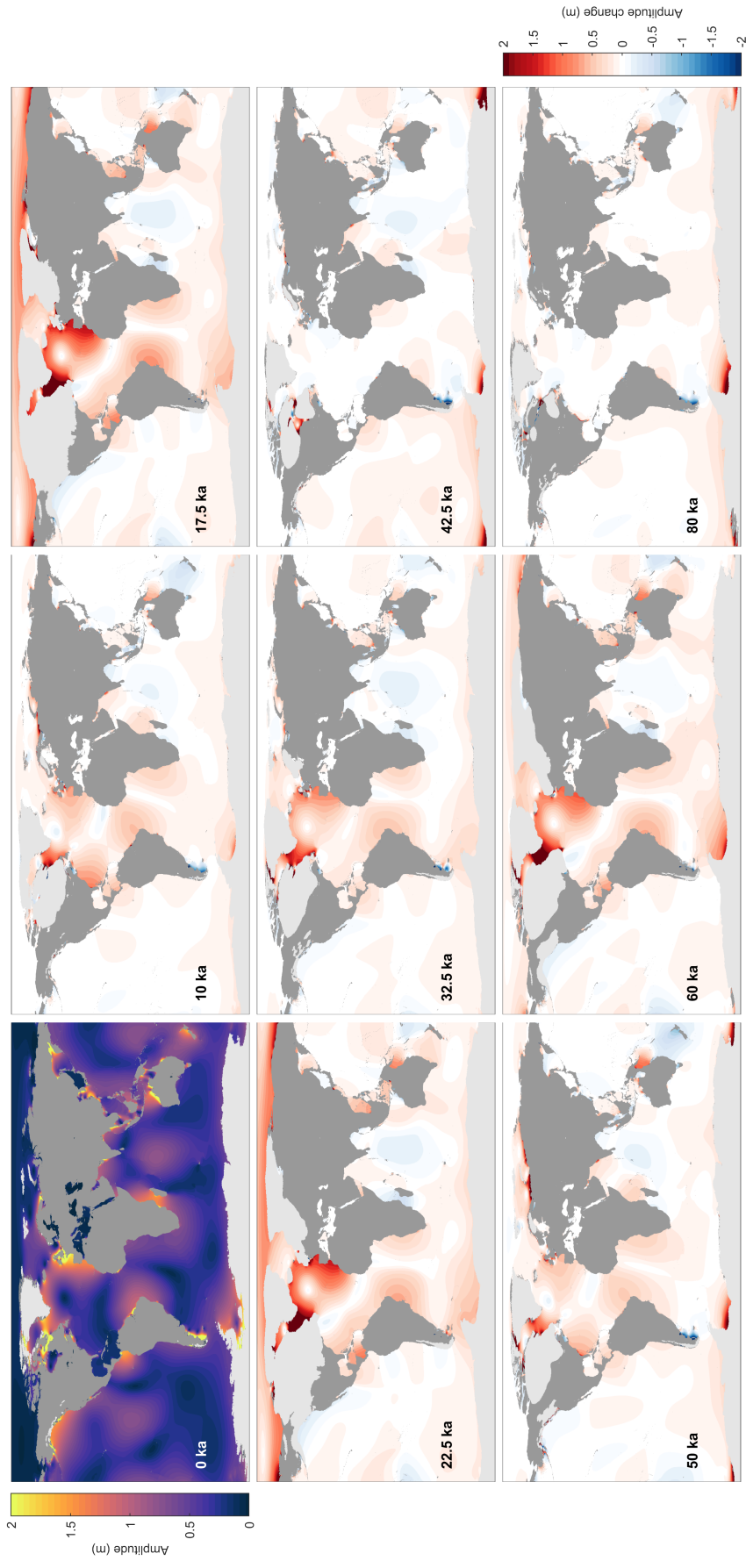


Figure 4. Same as Figure 3 but for the Gowan simulations

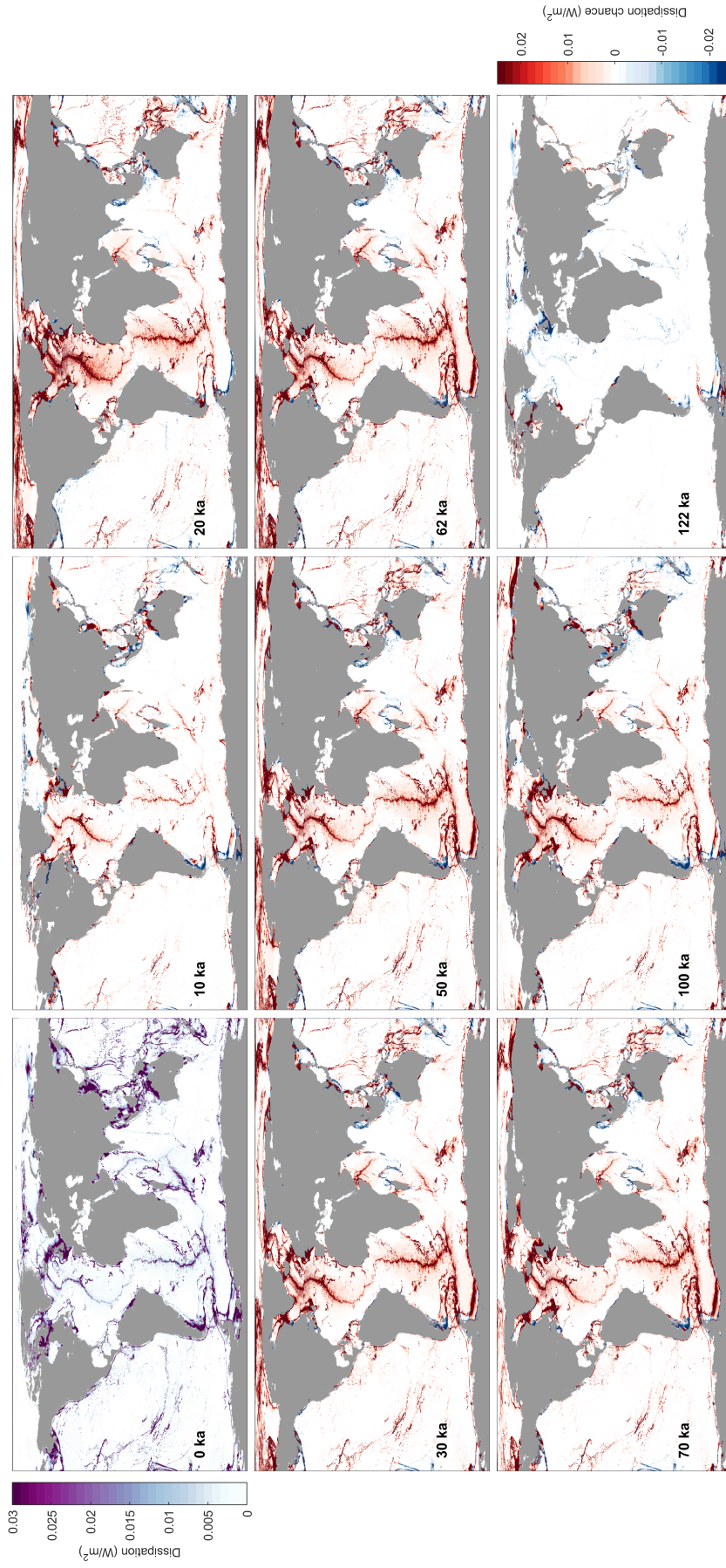


Figure 5. (top left panel) Present-day tidal dissipation plotted as the sum of the dissipation of the constituents M_2 , S_2 , K_1 and O_1 . (other panels) Dissipation (as sum of constituents M_2 , S_2 , K_1 and O_1) difference with respect to present for selected time slices over the last glacial cycle for the ICE-6G simulations. Land is shaded in grey.

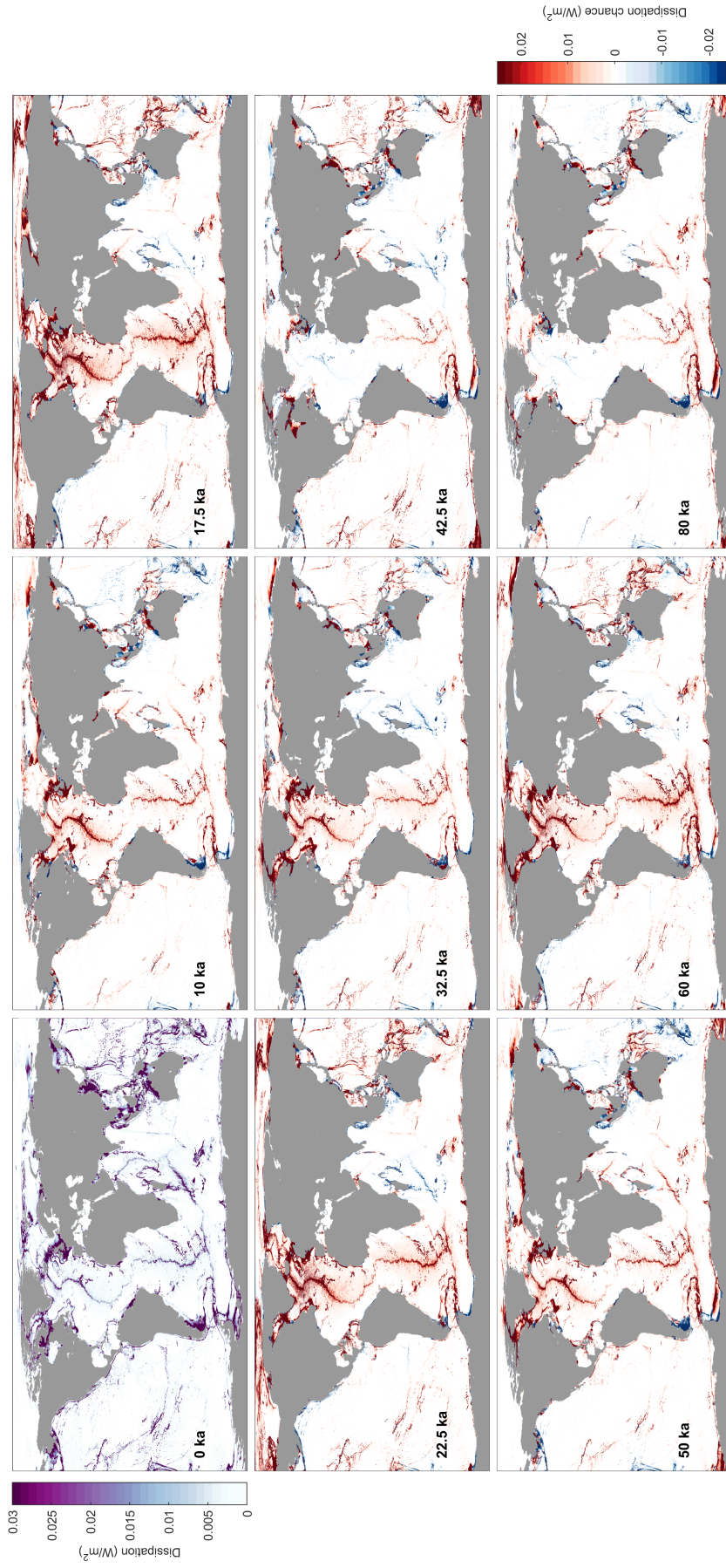


Figure 6. (top left) Present-day tidal dissipation plotted as the sum of the dissipation of the constituents M_2 , S_2 , K_1 and O_1 . (other panels) Dissipation (as sum of constituents M_2 , S_2 , K_1 and O_1) difference with respect to present for selected time slices over the last glacial cycle for the Gowan simulations. Land is shaded in grey.

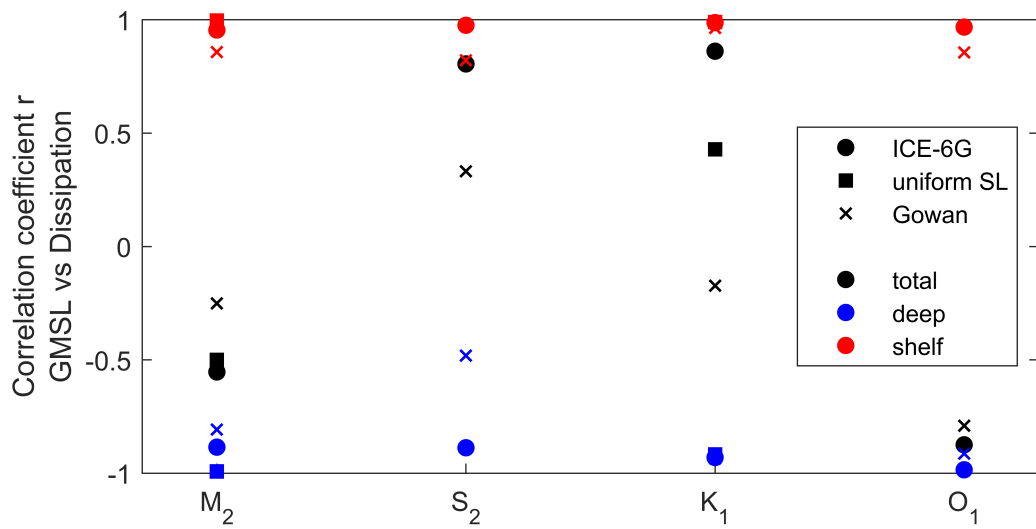


Figure 7. Correlation coefficients between GMSL and dissipation by tidal constituent from runs with ICE-6G bathymetry (circular markers), with uniform sea level changes (squares) and the Gowan bathymetries (crosses). Blue markers are used for open ocean dissipation, red ones for shelf sea dissipation and black ones for globally integrated dissipation.

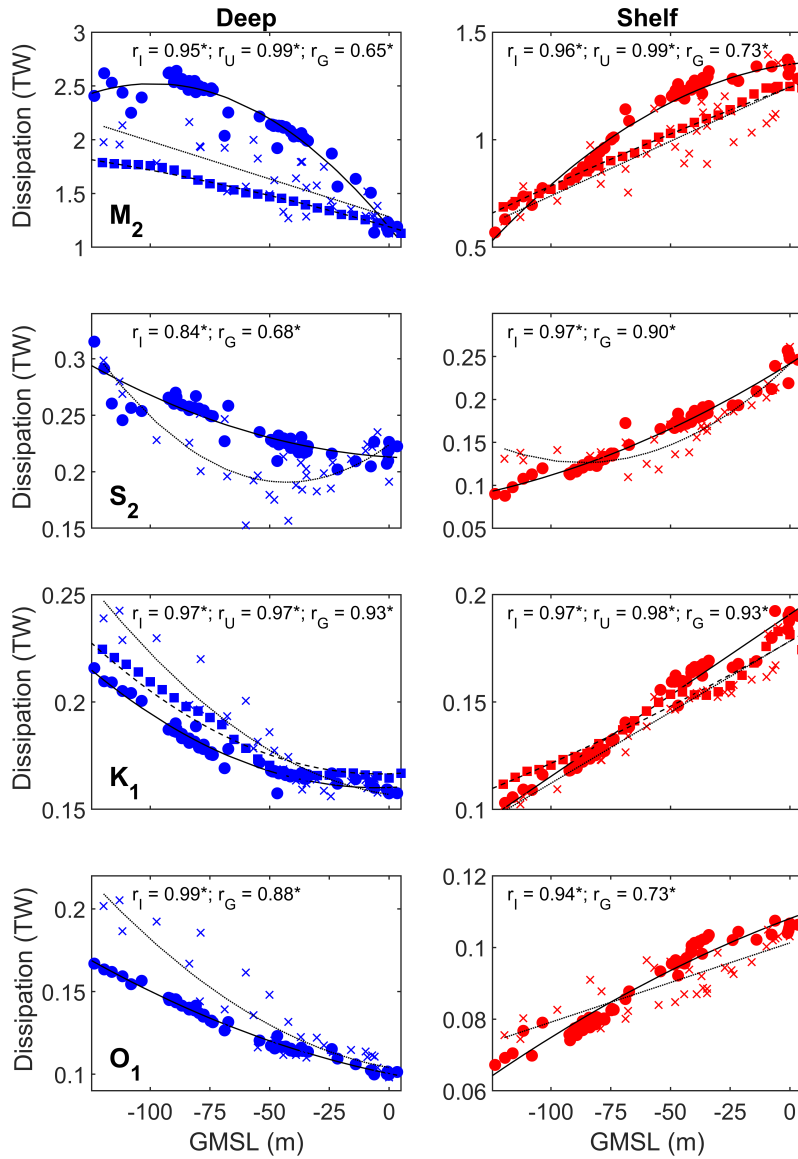


Figure 8. Open ocean dissipation (blue, left column) and shelf sea dissipation (red, right column) plotted against GMSL for the constituents M_2 , S_2 , K_1 and O_1 (top to bottom). Circular markers show dissipation from the ICE-6G simulations, Gowan simulations are shown with crosses, and squares plot dissipation from the uniform SL runs (M_2 and K_1 only). Regression lines are plotted in black (solid for ICE-6G and dashed for uniform SL runs). The correlation coefficients r between the explicitly modelled and regression-estimated dissipation values are printed in each panel for ICE-6G (r_I), the uniform SL simulations (r_U), and the Gowan simulations (r_G). Stars indicate that the correlation is significant at the 99% confidence level.

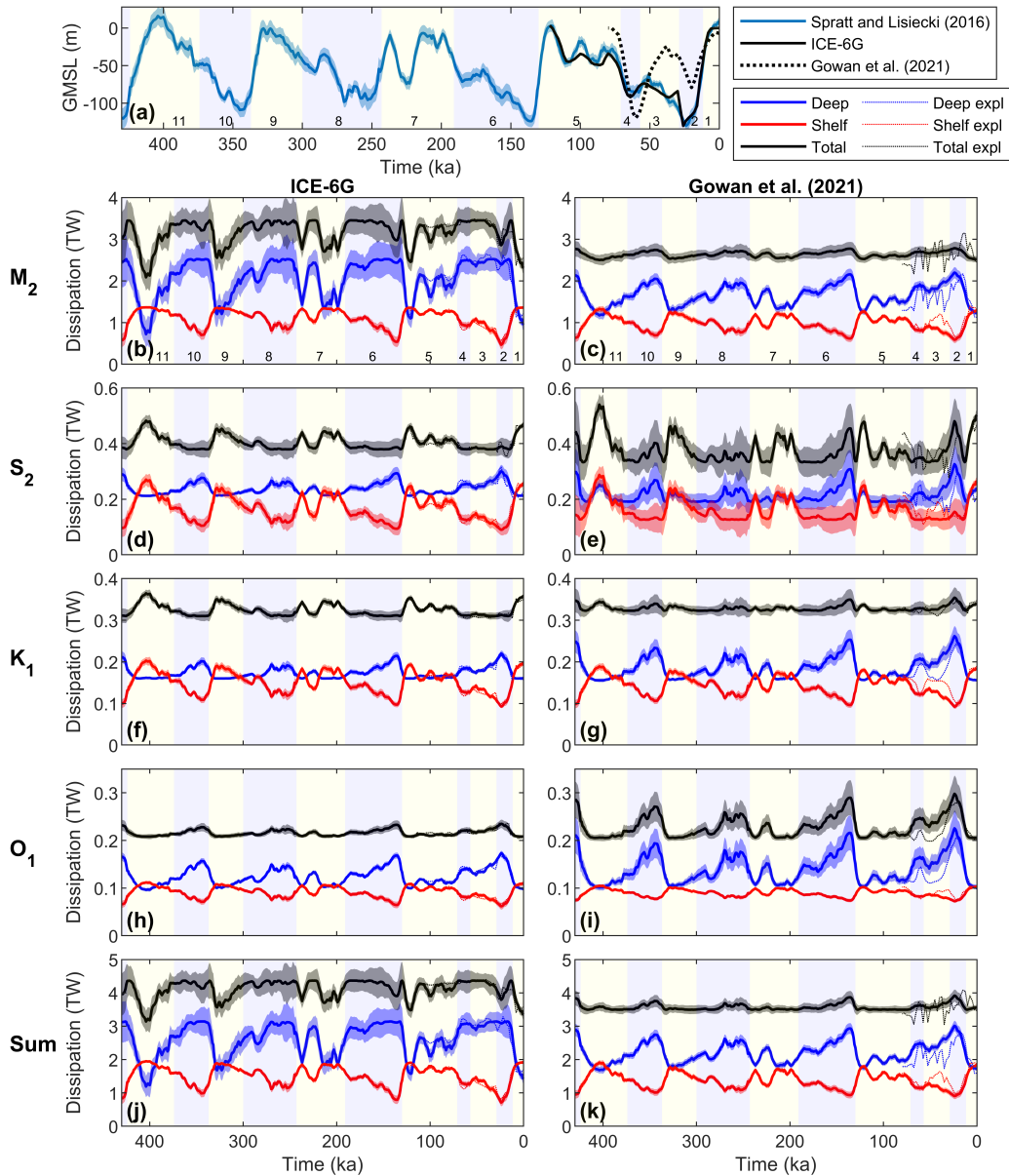


Figure 9. (a) Global mean sea level from the Spratt and Lisiecki (2016) reconstruction (blue line) with shading indicating upper and lower uncertainties, from the ICE-6G bathymetry (black solid line) and from Gowan et al. (2021) (black dotted line). Light blue and light yellow shading with corresponding numbering indicates Marine Isotope Stages. (b, d, f, h, j) Regression estimated dissipation for the constituents M_2 , S_2 , K_1 and O_1 , respectively, and the sum thereof. Open ocean (deep) dissipation is plotted in blue, shelf sea dissipation in red and globally integrated dissipation in black using the ICE-6G regression models. Shading indicates one standard deviation uncertainty of the dissipation estimates. Explicitly modelled dissipation values for the last glacial cycle are overlain in with dashed lines. Light blue and light yellow shading with corresponding numbering indicates Marine Isotope Stages. (c, e, g, i, j, k) same as (b, d, f, h, j) but for the Gowan et al. (2021) regression model.

References

- Anandakrishnan, S. (2003). Ice stream D flow speed is strongly modulated by the tide beneath the Ross Ice Shelf. *Geophysical Research Letters*, *30*(7), 1–4. doi: 10.1029/2002GL016329
- Anselin, J., Reed, B. C., Jenkins, A., & Green, J. A. (2023). Ice Shelf Basal Melt Sensitivity to Tide-Induced Mixing Based on the Theory of Subglacial Plumes. *Journal of Geophysical Research: Oceans*, *128*(4), e2022JC019156. doi: 10.1029/2022JC019156
- Arbic, B. K., Karsten, R. H., & Garrett, C. (2009). On tidal resonance in the global ocean and the back-effect of coastal tides upon open-ocean tides. *Atmosphere-Ocean*, *47*, 239–266. doi: 10.3137/OC311.2009
- Arbic, B. K., MacAyeal, D. R., Mitrovica, J. X., & Milne, G. A. (2004). Ocean tides and Heinrich events. *Nature*, *432*(7016), 460. doi: 10.1038/432460a
- Arbic, B. K., Mitrovica, J. X., MacAyeal, D. R., & Milne, G. A. (2008). On the factors behind large Labrador Sea tides during the last glacial cycle and the potential implications for Heinrich events. *Paleoceanography*, *23*, PA3211, doi:10.1029/2007PA001573.
- Argus, D. F., Peltier, W. R., Drummond, R., & Moore, A. W. (2014). The Antarctica component of postglacial rebound model ICE-6G_C (VM5a) based on GPS positioning, exposure age dating of ice thicknesses, and relative sea level histories. *Geophysical Journal International*, *198*(1), 537–563. doi: 10.1093/gji/ggu140
- Batchelor, C. L., Margold, M., Krapp, M., Murton, D. K., Dalton, A. S., Gibbard, P. L., Stokes, C. R., Murton, J. B., . . . Manica, J. A. (2019). The configuration of Northern Hemisphere ice sheets through the Quaternary. *Nature communications*, *10*(1), 3713–110. doi: 10.1038/s41467-019-11601-2
- Batchelor, C. L., Christie, F. D., Ottesen, D., Montelli, A., Evans, J., Dowdeswell, E. K., . . . Dowdeswell, J. A. (2023). Rapid, buoyancy-driven ice-sheet retreat of hundreds of metres per day. *Nature* *2023* *617*:7959, 617(7959), 105–110. doi: 10.1038/s41586-023-05876-1
- Bindschadler, R. a., King, M. a., Alley, R. B., Anandakrishnan, S., & Padman, L. (2003). Tidally controlled stick-slip discharge of a West Antarctic ice. *Science (New York, N.Y.)*, *301*(5636), 1087–9. doi: 10.1126/science.1087231
- Carless, S. J., Green, J. A., Pelling, H. E., & Wilmes, S. B. (2016). Effects of future sea-level rise on tidal processes on the Patagonian Shelf. *Journal of Marine Systems*, *163*, 113–124. doi: 10.1016/j.jmarsys.2016.07.007
- Clark, P. U., Dyke, A. S., Shakun, J. D., Carlson, A. E., Clark, J., Wohlfarth, B., . . . McCabe, A. M. (2009). The Last Glacial Maximum. *Science*, *325*(5941), 710–4. doi: 10.1126/science.1172873
- Creveling, J. R., Mitrovica, J. X., Clark, P. U., Waelbroeck, C., & Pico, T. (2017). Predicted bounds on peak global mean sea level during marine isotope stages 5a and 5c. *Quaternary Science Reviews*, *163*, 193–208. doi: https://doi.org/10.1016/j.quascirev.2017.03.003
- Dalton, A. S., Finkelstein, S. A., Barnett, P. J., & Forman, S. L. (2016). Constraining the Late Pleistocene history of the Laurentide Ice Sheet by dating the Missinaibi Formation, Hudson Bay Lowlands, Canada. *Quaternary Science Reviews*, *146*, 288–299. doi: 10.1016/j.quascirev.2016.06.015
- Dalton, A. S., Pico, T., Gowan, E. J., Clague, J. J., Forman, S. L., McMartin, I., . . . Helmens, K. F. (2022). The marine $\delta^{18}\text{O}$ record overestimates continental ice volume during Marine Isotope Stage 3. *Global and Planetary Change*, *212*, 103814. doi: 10.1016/j.gloplacha.2022.103814
- De Boer, B., Lourens, L. J., & Van De Wal, R. S. (2014). Persistent 400,000-year variability of antarctic ice volume and the carbon cycle is revealed throughout the plio-pleistocene. *Nature Communications*, *5*(1), 1–8. doi: 10.1038/ncomms3999
- Egbert, G. D. (2004). Numerical modeling of the global semidiurnal tide in the present day and in the last glacial maximum. *Journal of Geophysical Research*, *109*(C3), 1–15. doi: 10.1029/2003JC001973
- Egbert, G. D., Bills, B. G., & Ray, R. D. (2004). Numerical modeling of the global semidiurnal tide in the present day and in the last glacial maximum. *Journal of Geophysical Research*, *109*(C3), 1–15. doi: 10.1029/2003JC001973
- Ferrari, R., & Wunsch, C. (2009, jan). Ocean Circulation Kinetic Energy: Reservoirs, Sources, and Sinks. *Annual Review of Fluid Mechanics*, *41*(1), 253–282. doi: 10.1146/annurev.fluid.40

- .111406.102139
- 610
611 Fox-Kemper, B., Helene T. Hewitt, Cunde Xiao, Guðfinna Aðalgeirsdóttir, Sybren S. Drijfhout,
612 Tamsin L. Edwards, . . . et al. (2021). Ocean, Cryosphere and Sea Level Change. In
613 *Climate change 2021: The physical science basis. contribution of working group i to the sixth*
614 *assessment report of the intergovernmental panel on climate change* (pp. 1211–1362).
- 615 Gomez, N., Weber, M. E., Clark, P. U., Mitrovica, J. X., & Han, H. K. (2020). Antarctic ice dynamics
616 amplified by Northern Hemisphere sea-level forcing. *Nature* 2020 587:7835, 587(7835), 600–
617 604. doi: 10.1038/s41586-020-2916-2
- 618 Gowan, E. J., Zhang, X., Khosravi, S., Rovere, A., Stocchi, P., Hughes, A. L. C., . . . Lohmann, G.
619 (2021). A new global ice sheet reconstruction for the past 80.000 years. *Nature Communica-*
620 *tions*, 12(1), 1199. doi: 10.1038/s41467-021-21469-w
- 621 Grant, K. M., Rohling, E. J., Bronk Ramsey, C., Cheng, H., Edwards, R. L., Florindo, F., . . .
622 Williams, F. (2014). Sea-level variability over five glacial cycles. *Nature Communications*,
623 5(1), 1–9. doi: 10.1038/ncomms6076
- 624 Green, J. A. (2010). Ocean tides and resonance. *Ocean Dynamics*, 60(5), 1243–1253. doi:
625 10.1007/s10236-010-0331-1
- 626 Green, J. A., & Huber, M. (2013). Tidal dissipation in the early Eocene and implications for ocean
627 mixing. *Geophysical Research Letters*, 40(11), 2707–2713. doi: 10.1002/grl.50510
- 628 Green, J. A., Huber, M., Waltham, D., Buzan, J., & Wells, M. (2017). Explicitly modelled deep-time
629 tidal dissipation and its implication for Lunar history. *Earth and Planetary Science Letters*,
630 461, 46–53. doi: 10.1016/j.epsl.2016.12.038
- 631 Green, J. A. M., & Nycander, J. (2013). A Comparison of Tidal Conversion Parameterizations for
632 Tidal Models. *Journal of Physical Oceanography*, 43(1), 104–119. doi: 10.1175/JPO-D-12
633 -023.1
- 634 Griffiths, S. D., & Peltier, W. R. (2008). Megatides in the Arctic Ocean under glacial conditions.
635 *Geophysical Research Letters*, 35, L08605, doi:10.1029/2008GL033263.
- 636 Griffiths, S. D., & Peltier, W. R. (2009). Modeling of polar ocean tides at the Last Glacial Maximum:
637 amplification, sensitivity, and climatological implications. *Journal of Climate*, 22, 2905–2924.
638 doi: 10.1175/2008JCLI2540.1
- 639 Gudmundsson, G. H. (2007). Tides and the flow of Rutford Ice Stream, West Antarctica. *J. Geophys.*
640 *Res.*, 112(F4), F04007. doi: 10.1029/2006JF000731
- 641 Hayden, A. M., Wilmes, S. B., Gomez, N., Green, J. A., Pan, L., Han, H., & Golledge, N. R.
642 (2020). Multi-Century Impacts of Ice Sheet Retreat on Sea Level and Ocean Tides in Hudson
643 Bay. *Journal of Geophysical Research: Oceans*, 125(11), e2019JC015104. doi: 10.1029/
644 2019JC015104
- 645 Hendershott, M. C. (1972). The effects of solid earth deformation on global ocean tides. *Geophysical*
646 *Journal of the Royal Astronomic Society*, 29, 389–402.
- 647 Kendall, R. A., Mitrovica, J. X., & Milne, G. A. (2005). On post-glacial sea level – II. Numerical
648 formulation and comparative results on spherically symmetric models. *Geophysical Journal*
649 *International*, 161(3), 679–706. doi: 10.1111/J.1365-246X.2005.02553.X
- 650 Lambeck, K. (2004). Sea-level change through the last glacial cycle: geophysical, glaciological
651 and palaeogeographic consequences. *Comptes Rendus Geoscience*, 336(7), 677–689. doi:
652 https://doi.org/10.1016/j.crte.2003.12.017
- 653 Lambeck, K., Rouby, H., Purcell, A., Sun, Y., & Sambridge, M. (2014). Sea level and global
654 ice volumes from the Last Glacial Maximum to the Holocene. *Proceedings of the National*
655 *Academy of Sciences of the United States of America*, 111(43), 15296–15303. doi: 10.1073/
656 pnas.1411762111
- 657 Menviel, L., Timmermann, A., Elison Timm, O., & Mouchet, A. (2017). Deconstructing the Last
658 Glacial termination: the role of millennial and orbital-scale forcings. *Quaternary Science*
659 *Reviews*, 30(9–10), 1155–1172. doi: 10.1016/j.quascirev.2011.02.005
- 660 Milillo, P., Rignot, E., Mouginot, J., Scheuchl, B., Morlighem, M., Li, X., & Salzer, J. T. (2017). On
661 the Short-term Grounding Zone Dynamics of Pine Island Glacier, West Antarctica, Observed
662 With COSMO-SkyMed Interferometric Data. *Geophysical Research Letters*, 44(20), 10,436–
663 10,444. doi: 10.1002/2017GL074320
- 664 Milne, G. A., & Mitrovica, J. X. (1996). Postglacial sea-level change on a rotating Earth: first results

- 665 from a gravitationally self-consistent sea-level equation. *Geophysical Journal International*,
666 126(3), F13–F20. doi: 10.1111/j.1365-246X.1996.tb04691.x
- 667 Mitrovica, J. X., & Milne, G. A. (2003). On post-glacial sea level: I. General theory. *Geophysical*
668 *Journal International*, 154(2), 253–267. doi: 10.1046/J.1365-246X.2003.01942.X
- 669 Olinger, S. D., Lipovsky, B. P., Wiens, D. A., Aster, R. C., Bromirski, P. D., Chen, Z., . . . Stephen,
670 R. A. (2019). Tidal and Thermal Stresses Drive Seismicity Along a Major Ross Ice Shelf Rift.
671 *Geophysical Research Letters*, 46(12), 6644–6652. doi: 10.1029/2019GL082842
- 672 Peltier, W. R., Argus, D. F., & Drummond, R. (2015). Space geodesy constrains ice age terminal
673 deglaciation: The global ICE-6G-C (VM5a) model. *Journal of Geophysical Research: Solid*
674 *Earth*, 120(1), 450–487. doi: 10.1002/2014JB011176
- 675 Pickering, M. D., Horsburgh, K. J., Blundell, J. R., Hirschi, J. J., Nicholls, R. J., Verlaan, M., &
676 Wells, N. C. (2017). The impact of future sea-level rise on the global tides. *Continental Shelf*
677 *Research*, 142, 50–68. doi: 10.1016/j.csr.2017.02.004
- 678 Pico, T., Mitrovica, J. X., Ferrier, K. L., & Braun, J. (2016). Global ice volume during MIS 3 inferred
679 from a sea-level analysis of sedimentary core records in the Yellow River Delta. *Quaternary*
680 *Science Reviews*, 152, 72–79. doi: 10.1016/j.quascirev.2016.09.012
- 681 Pico, T., Creveling, J. R., & Mitrovica, J. X. (2017). Sea-level records from the U.S. mid-Atlantic
682 constrain Laurentide Ice Sheet extent during Marine Isotope Stage 3. *Nature Communications*,
683 8(1), 1–6. doi: 10.1038/ncomms15612
- 684 Pöppelmeier, F., Jeltsch-Thömmes, A., Lippold, J., Joos, F., & Stocker, T. F. (2023). Multi-proxy
685 constraints on Atlantic circulation dynamics since the last ice age. *Nature Geosciences*, 16,
686 349–356. doi: 10.1038/s41561-023-01140-3
- 687 Ray, R. D., Rowlands, D. D., & Egbert, G. D. (2003). Tidal models in a new era of satellite
688 gravimetry. *Space Science Reviews*, 108, 271–282.
- 689 Rohling, E. J., Grant, K., Bolshaw, M., Roberts, A. P., Siddall, M., Hemleben, C., & Kucera, M.
690 (2009). Antarctic temperature and global sea level closely coupled over the past five glacial
691 cycles. doi: 10.1038/ngeo557
- 692 Schaffer, J., Timmermann, R., Erik Arndt, J., Savstrup Kristensen, S., Mayer, C., Morlighem,
693 M., & Steinhage, D. (2016). A global, high-resolution data set of ice sheet topography,
694 cavity geometry, and ocean bathymetry. *Earth System Science Data*, 8(2), 543–557. doi:
695 10.5194/essd-8-543-2016
- 696 Schmittner, A., Green, J. A., & Wilmes, S. B. (2015). Glacial ocean overturning intensified by tidal
697 mixing in a global circulation model. *Geophysical Research Letters*, 42(10), 4014–4022. doi:
698 10.1002/2015GL063561
- 699 Shakun, J. D., Lea, D. W., Lisiecki, L. E., & Raymo, M. E. (2015). An 800-kyr record of
700 global surface ocean $\delta^{18}\text{O}$ and implications for ice volume-temperature coupling. *Earth and*
701 *Planetary Science Letters*, 426, 58–68. doi: 10.1016/j.epsl.2015.05.042
- 702 Siddall, M., Rohling, E. J., Almogi-Labin, A., Hemleben, C., Meischner, D., Schmelzer, I., & Smeed,
703 D. A. (2003). Sea-level fluctuations during the last glacial cycle. *Nature*, 423(6942), 853–858.
704 doi: 10.1038/nature01690
- 705 Simpson, J. H., & Pingree, R. D. (1978). Shallow sea fronts produced by tidal stirring. In *Oceanic*
706 *fronts in coastal processes: Proceedings of a workshop held at the marine sciences research*
707 *center, may 25–27, 1977* (pp. 29–42).
- 708 Spada, G., & Stocchi, P. (2007). SELEN: A Fortran 90 program for solving the “sea-level equation”.
709 *Computers & Geosciences*, 33(4), 538–562. doi: 10.1016/J.CAGEO.2006.08.006
- 710 Spratt, R. M., & Lisiecki, L. E. (2016). A Late Pleistocene sea level stack. *Climate of the Past*,
711 12(4), 1079–1092. doi: 10.5194/cp-12-1079-2016
- 712 Sulzbach, R., Klemann, V., Knorr, G., Dobslaw, H., Dümpelmann, H., Lohmann, G., & Thomas, M.
713 (2023). Evolution of global ocean tide levels since the Last Glacial Maximum. *Paleoceanog-*
714 *raphy and Paleoclimatology*, 38, e2022PA004556. doi: 10.1029/2022PA004556
- 715 Thomas, H., Bozec, Y., Elkalay, K., & de Baar, H. J. W. (2004). Enhanced open ocean storage of
716 CO₂ from shelf sea pumping. *Science (New York, N.Y.)*, 304(5673), 1005–8. doi: 10.1126/
717 science.1095491
- 718 Uehara, K., Scourse, J. D., Horsburgh, K. J., Lambeck, K., & Purcell, A. P. (2006). Tidal evolution
719 of the northwest European shelf seas from the Last Glacial Maximum to the present. *Journal*

- 720 *of Geophysical Research*, *111*, C09025, doi: 10.1029/2006JC003531.
- 721 Velay-Vitow, J., Peltier, W. R., & Stuhne, G. R. (2020). The Tides of the Glacial Ocean and Their
722 Possible Connection to Heinrich Event Instabilities of the Laurentide Ice Sheet. *Journal of*
723 *Geophysical Research: Oceans*, *125*(1). doi: 10.1029/2019JC015444
- 724 Waelbroeck, C., Labeyrie, L., Michel, E., Duplessy, J. C., McManus, J. F., Lambeck, K., ...
725 Labracherie, M. (2002). Sea-level and deep water temperature changes derived from benthic
726 foraminifera isotopic records. *Quaternary Science Reviews*, *21*(1), 295–305. doi: [https://doi.org/10.1016/S0277-3791\(01\)00101-9](https://doi.org/10.1016/S0277-3791(01)00101-9)
- 727
728 Walker, R. T., Parizek, B. R., Alley, R. B., Anandakrishnan, S., Riverman, K. L., & Christianson, K.
729 (2013). Ice-shelf tidal flexure and subglacial pressure variations. *Earth and Planetary Science*
730 *Letters*, *361*, 422–428. doi: 10.1016/J.EPSL.2012.11.008
- 731 Ward, S. L., Neill, S. P., Scourse, J. D., Bradley, S. L., & Uehara, K. (2016). Sensitivity of
732 palaeotidal models of the northwest European shelf seas to glacial isostatic adjustment since
733 the Last Glacial Maximum. *Quaternary Science Reviews*, *151*, 198–211. doi: <https://doi.org/10.1016/j.quascirev.2016.08.034>
- 734
735 Wilmes, S. B., & Green, J. A. (2014). The evolution of tides and tidal dissipation over the
736 past 21,000 years. *Journal of Geophysical Research: Oceans*, *119*(7), 4083–4100. doi:
737 10.1002/2013JC009605
- 738 Wilmes, S. B., Green, J. A., Gomez, N., Rippeth, T. P., & Lau, H. (2017). Global Tidal Impacts
739 of Large-Scale Ice Sheet Collapses. *Journal of Geophysical Research: Oceans*, *122*(11),
740 8354–8370. doi: 10.1002/2017JC013109
- 741 Wilmes, S.-B., Green, J. A. M., & Schmittner, A. (2021). Enhanced vertical mixing in the glacial
742 ocean inferred from sedimentary carbon isotopes. *Communications Earth & Environment*,
743 *2*(1), 166. doi: 10.1038/s43247-021-00239-y
- 744 Wilmes, S. B., Schmittner, A., & Green, J. A. (2019). Glacial Ice Sheet Extent Effects on Modeled
745 Tidal Mixing and the Global Overturning Circulation. *Paleoceanography and Paleoclimatol-*
746 *ogy*, *34*(8), 1437–1454. doi: 10.1029/2019PA003644
- 747 Wilmes, S. B., Ward, S., & Uehara, K. (2022). Present day: Tides in a changing climate. In *A*
748 *journey through tides* (pp. 185–229). Elsevier. doi: 10.1016/B978-0-323-90851-1.00009-1
- 749 Wilmes, S. B., Pedersen, V. K., Schindelegger, M., & Green, J. A. (2023). Late Pleistocene
750 evolution of tides and tidal dissipation: tidal simulations [Dataset]. *Zenodo*. doi: 10.5281/
751 zenodo.8147509
- 752 Wunsch, C., & Ferrari, R. (2004). Vertical mixing, energy, and the general circulation of the oceans.
753 *Annual Review of Fluid Mechanics*, *36*, 281–314, doi:10.1146/annurev.fluid.36.050802.
- 754 Zaron, E. D., & Egbert, G. D. (2006). Estimating open-ocean barotropic tidal dissipation: The
755 Hawaiian Ridge. *Journal of Physical Oceanography*, *36*, 1019–1035.